AGU PUBLICATIONS

JGR

Journal of Geophysical Research: Planets

RESEARCH ARTICLE
10.1002/2016JE005225

Key Points:
- The SAM instrument has detected evolved water, H2, SO2, H2S, NO, CO_2, CO, O_2, and HCl from Gale Crater sediments and sedimentary rock
- SAM detections are consistent with the presence of nitrate, organic C, carbonate, phyllosilicates, perchlorate, chlorate, and sulfate
- Gale Crater materials have experienced a complex authigenetic/diagenetic history with fluids of varying pH, redox, and salt composition

Supporting Information:
- Supporting Information S1

Correspondence to:
B. Sutter,
brad.sutter-2@nasa.gov

Citation:
Sutter, B., et al. (2017), Evolved gas analyses of sedimentary rocks and eolian sediment in Gale Crater, Mars: Results of the Curiosity rover's sample analysis at Mars instrument from Yellowknife Bay to the Namib Dune, *J. Geophys. Res. Planets*, *122*, 2574–2609, doi:10.1002/2016JE005225.

Received 18 NOV 2016
Accepted 6 JUL 2017
Accepted article online 12 JUL 2017
Published online 7 DEC 2017

Evolved gas analyses of sedimentary rocks and eolian sediment in Gale Crater, Mars: Results of the Curiosity rover's sample analysis at Mars instrument from Yellowknife Bay to the Namib Dune

B. Sutter[1,2], A. C. McAdam[3], P. R. Mahaffy[3], D. W. Ming[2], K. S. Edgett[4], E. B. Rampe[2], J. L. Eigenbrode[3], H. B. Franz[3], C. Freissinet[5], J. P. Grotzinger[6], A. Steele[7], C. H. House[8], P. D. Archer[1,2], C. A. Malespin[3], R. Navarro-González[9], J. C. Stern[3], J. F. Bell[10], F. J. Calef[11], R. Gellert[12], D. P. Glavin[3], L. M. Thompson[13], and A. S. Yen[11]

[1]Jacobs Technology, Houston, Texas, USA, [2]NASA Johnson Space Center, Houston, Texas, USA, [3]NASA Goddard Space Flight Center, Greenbelt, Maryland, USA, [4]Malin Space Science Systems, San Diego, California, USA, [5]LATMOS-IPSL, CNRS-Guyancourt, Guyancourt, France, [6]Division of Geologic and Planetary Sciences, California Institute of Technology, Pasadena, California, USA, [7]Geophysical Laboratory, Carnegie Institution of Washington, Washington, District of Columbia, USA, [8]Department of Geosciences, Pennsylvania State University, University Park, Pennsylvania, USA, [9]Instituto de Ciencias Nucleares, Universidad Nacional Autónoma de México, Ciudad Universitaria, México City, Mexico, [10]School of Earth and Space Exploration, Arizona State University, Tempe, Arizona, USA, [11]Jet Propulsion Laboratory, California Institute of Technology, Pasadena, California, USA, [12]Guelph-Waterloo Physics Institute, University of Guelph, Guelph, Ontario, Canada, [13]Planetary and Space Science Centre, University of New Brunswick, Fredericton, New Brunswick, Canada

Abstract The sample analysis at Mars instrument evolved gas analyzer (SAM-EGA) has detected evolved water, H_2, SO_2, H_2S, NO, CO_2, CO, O_2, and HCl from two eolian sediments and nine sedimentary rocks from Gale Crater, Mars. These evolved gas detections indicate nitrates, organics, oxychlorine phase, and sulfates are widespread with phyllosilicates and carbonates occurring in select Gale Crater materials. Coevolved CO_2 (160 ± 248–2373 ± 820 $\mu gC_{(CO2)}/g$) and CO (11 ± 3–320 ± 130 $\mu gC_{(CO)}/g$) suggest that organic C is present in Gale Crater materials. Five samples evolved CO_2 at temperatures consistent with carbonate (0.32 ± 0.05–0.70 ± 0.1 wt % CO_3). Evolved NO amounts to 0.002 ± 0.007–0.06 ± 0.03 wt % NO_3. Evolution of O_2 suggests that oxychlorine phases (chlorate/perchlorate) (0.05 ± 0.025–1.05 ± 0.44 wt % ClO_4) are present, while SO_2 evolution indicates the presence of crystalline and/or poorly crystalline Fe and Mg sulfate and possibly sulfide. Evolved H_2O (0.9 ± 0.3–2.5 ± 1.6 wt % H_2O) is consistent with the presence of adsorbed water, hydrated salts, interlayer/structural water from phyllosilicates, and possible inclusion water in mineral/amorphous phases. Evolved H_2 and H_2S suggest that reduced phases occur despite the presence of oxidized phases (nitrate, oxychlorine, sulfate, and carbonate). SAM results coupled with CheMin mineralogical and Alpha-Particle X-ray Spectrometer elemental analyses indicate that Gale Crater sedimentary rocks have experienced a complex authigenetic/diagenetic history involving fluids with varying pH, redox, and salt composition. The inferred geochemical conditions were favorable for microbial habitability and if life ever existed, there was likely sufficient organic C to support a small microbial population.

1. Introduction

The Mars Science Laboratory (MSL) Curiosity rover and its payload of science instruments have traversed ~12 km for 1237 Martian solar days (sols) spanning more than 100 m of sedimentary stratigraphy. Along the way, Curiosity has evaluated the sedimentology, geomorphology, geochemistry, and mineralogy of regolith fines, eolian sediments, sedimentary rocks, and igneous clasts in the sedimentary rocks of Gale Crater [e.g., *Meslin et al.*, 2013; *Minitti et al.*, 2013; *Williams et al.*, 2013; *McLennan et al.*, 2014; *Ming et al.*, 2014; *Schmidt et al.*, 2014; *Vaniman et al.*, 2014; *Cousin et al.*, 2015; *Grotzinger et al.*, 2015] (Figures 1 and 2). Gale Crater is ~155 km wide with an ~5 km high layered central mound (Aeolis Mons; informally known as Mount Sharp) [*Malin and Edgett*, 2000; *Grotzinger et al.*, 2015]. Orbiting infrared analyses suggest that the lower slopes (<1 km) of Mount Sharp consist of strata that contain variable amounts of hematite, phyllosilicates, and sulfate [*Milliken et al.*, 2010]. The remaining upper several kilometers of Mount Sharp strata do not present infrared signatures that can be interpreted in terms of mineral components. Spectral evidence for minerals on upper Mount Sharp in some cases may be obscured by dust [*Milliken et al.*, 2010]. Limitations in spatial

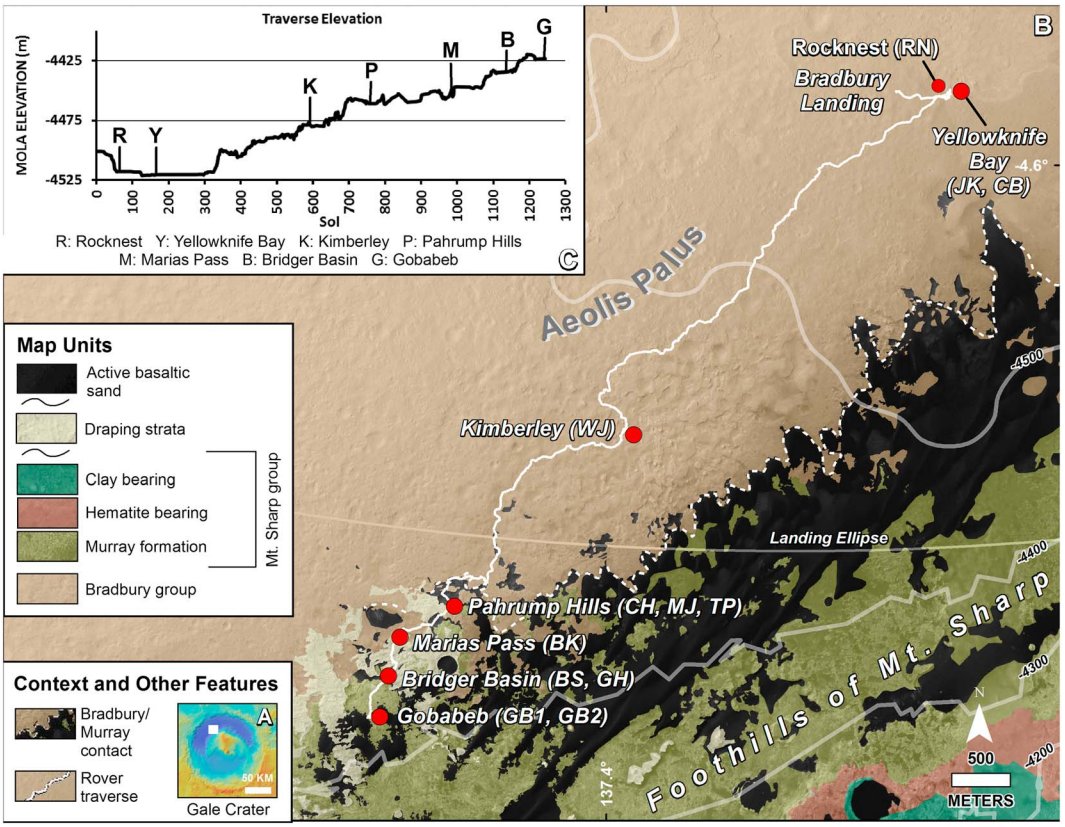

Figure 1. Regional geologic map, on Mars Reconnaissance Orbiter (MRO) High Resolution Imaging Experiment (HiRISE) camera image mosaic base map, showing the Curiosity rover traverse (white line) and sampling sites. (a) Gale Crater topography; the white box outlines the area shown in Figure 1b. (b) Geologic map showing the principal stratigraphic units exposed at Aeolis Palus and the foothills of Aeolia Mons (Mount Sharp) and the sample sites (red dots) with individual sample abbreviations (in parentheses) along the rover traverse where SAM analyses were conducted through sol 1237. (c) Topographic profile of the rover traverse.

coverage and resolution, dust cover, and the types and abundances of minerals that can be detected by a given orbital observing technique mean that there is an incomplete understanding of the compositional variations within Mount Sharp strata. Results from MSL investigations are intended to enhance our understanding of the composition of Mount Sharp and to search for records of past or evidence of present geochemical and environmental conditions that could have been suitable for microbial activity [*Grotzinger et al.*, 2014, 2015].

Current estimates place Gale Crater formation at ~3.8 to 3.6 billion years ago with deposition of sedimentary material occurring until ~3.3 to 3.1 billion years ago [e.g., *Thomson et al.*, 2011; *Schwenzer et al.*, 2012; *Grotzinger et al.*, 2015]. The sedimentary rock strata encountered along the rover's traverse are interpreted to record interfingered fluvial, deltaic, and lacustrine environments. This indicates that Gale Crater had intermittent bodies of standing water that could have lasted from 100 to 10,000 years on the surface [*Grotzinger et al.*, 2014, 2015].

The sample analysis at Mars (SAM) instrument has been essential in providing a fundamental understanding of the volatile-bearing phases including organic materials in Gale Crater sediments. The SAM analyses of the scooped eolian drift material (Rocknest-RN) and two drilled lacustrine mudstone samples of the Sheepbed member at the base of the Bradbury group (Figure 2; John Klein-JK and Cumberland-CB) have resulted in reporting the detection of evolved water, SO_2, H_2S, CO_2, NO, O_2, HCl, and organics [*Glavin et al.*, 2013; *Leshin et al.*, 2013; *Archer et al.*, 2014; *Ming et al.*, 2014; *McAdam et al.*, 2014; *Freissinet et al.*, 2015; *Stern et al.*, 2015, 2017]. SAM results demonstrated that water was likely adsorbed to particle surfaces and also associated with amorphous phases, phyllosilicates, and hydrated salts [*Leshin et al.*, 2013; *Ming et al.*, 2014].

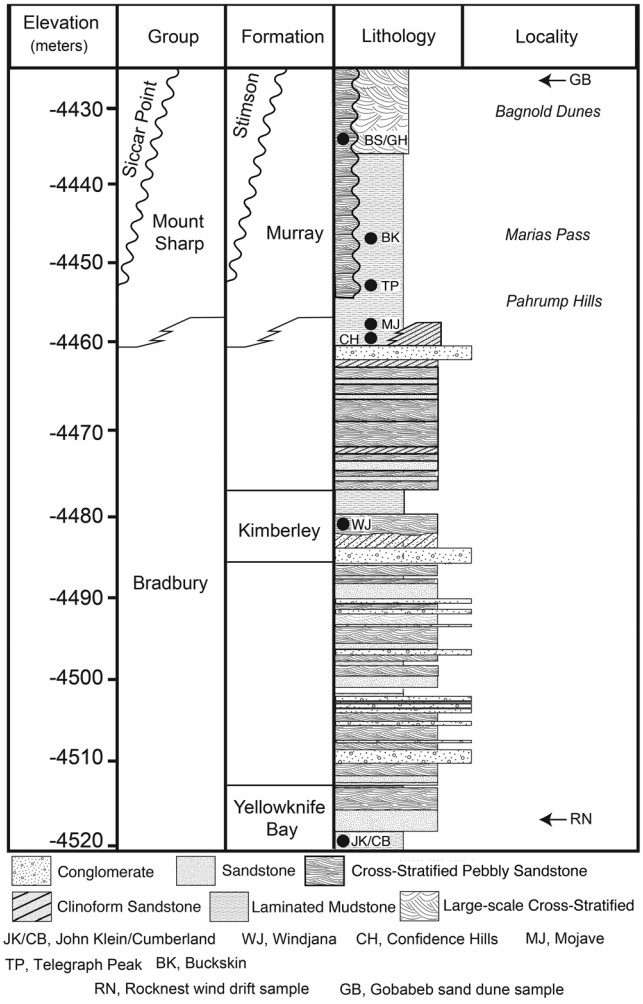

Figure 2. Stratigraphic column describing the sedimentary facies from Yellowknife Bay to Stimson formation. The Bradbury (Aeolis Palus) group and the Murray formation contact is composed of interfingering facies. Stimson formation uncomformably overlies Murray formation. The Rocknest (RN) and Gobabeb (GB) are loose, unconsolidated modern eolian sediments that overlie the Yellowknife Bay and Murray formations, respectively. See *Grotzinger et al.* [2015] for detailed stratigraphic discussion.

Iron sulfates, amorphous S phases, and possible oxidation of iron sulfides are likely sources of SO_2 [*McAdam et al.*, 2014]. Oxygen and HCl releases are consistent with the presence of perchlorate and chlorate phases [*Glavin et al.*, 2013; *Ming et al.*, 2014; *Sutter et al.*, 2016]. Organics, carbonates, and along with some contributions from instrument background are possible sources of evolved CO_2 [*Glavin et al.*, 2013; *Leshin et al.*, 2013; *Ming et al.*, 2014; *Freissinet et al.*, 2015]. Another significant discovery was the first in situ detection of nitrate on Mars in the Gale Crater sediments [*Stern et al.*, 2015]. Nitrate has been detected in Martian meteorites [*Kounaves et al.*, 2014]; however, the SAM detection confirms the presence of nitrate on Mars. This discovery in sedimentary rocks and eolian sediments indicates nitrogen (N) was present for potential microbial activity on Mars.

Results from the SAM instrument have indicated that Gale Crater sediments consist of oxidized (sulfate, nitrate, and oxychlorine) and reduced (sulfides and organics) phases along with minerals that formed in acidic (e.g., Fe sulfate) and alkaline (e.g., phyllosilicate and carbonate) conditions [e.g., *Leshin et al.*, 2013; *McAdam et al.*, 2014; *McLennan et al.*, 2014; *Ming et al.*, 2014; *Rampe et al.*, 2017]. The CheMin X-ray diffraction instrument has verified the SAM detections of phyllosilicates, iron sulfides, and iron sulfate (e.g., jarosite) [*Vaniman et al.*, 2014; *Hurowitz et al.*, 2017; *Rampe et al.*, 2017]. These results indicate that sedimentary rocks in Gale Crater are composed of complex mineral mixtures that reflect varying geochemical conditions at likely different times, represented by mineral inventories at different stratigraphic levels. These mineral mixtures suggest that past geochemical conditions may have been favorable for microbial life [e.g., *Grotzinger et al.*, 2014]. Some mineral assemblages are out of equilibrium, for example, at the base of Murray formation at Pahrump hills where iron sulfate minerals coexist with phyllosilicate minerals [*Hurowitz et al.*, 2017; *Rampe et al.*, 2017], which demonstrates that these samples may preserve evidence of multiple aqueous episodes.

The goal of this work is to provide a comprehensive summary of all major evolved gases detected in samples analyzed by the SAM evolved gas analyzer (SAM-EGA). The SAM-EGA data of RN, JK, and CB samples have been previously reported [e.g., *Leshin et al.*, 2013; *Ming et al.*, 2014] and are included here with the eight additional sampling sites to provide a complete summary of results. The objectives of this work are to (1) provide a comprehensive characterization of the evolved gas (H_2O, SO_2, H_2S, CO_2, CO, NO, O_2, HCl, and H_2) release from samples analyzed by SAM since landing (sol 0) to the analysis of eolian dune material at Gobabeb (GB) (sol 1237), (2) place constraints on the mineralogy or composition of volatile-bearing phases based on

SAM-EGA, (3) highlight notable SAM-EGA detections along the MSL-rover traverse to enhance the understanding of the origins and compositions of Gale Crater sediments and sedimentary rock, and (4) discuss the implications of these results as related to the geochemical history and its impact on past microbial habitability in Gale Crater.

2. Materials and Methods

2.1. Sample Analysis at Mars (SAM) Instrument

The sample analysis at Mars (SAM) instrument analyzed evolved gases from Gale sediments with three instruments: the quadrupole mass spectrometer (MS), gas chromatograph (GC), and tunable laser spectrometer (TLS) [*Mahaffy et al.*, 2012]. Before sample acquisition, a SAM quartz sample cup was preconditioned to 870°C (5 min), and gas transfer lines and manifolds were preconditioned to 135°C (150 min) in order to minimize background contributions to the SAM analysis. Single or triple portions of scooped or drilled materials were transferred from Curiosity's sample processing system into quartz sample cups which are then sealed in a SAM oven. Samples were heated (35°C min^{-1}) to ~870°C where helium carrier gas flows (~0.8 cm^3 min^{-1} STP; 25 mbar) up through the porous quartz frit of the cup and flushes the evolved volatiles from the sample to the MS. As the sample was heated, gases (e.g., H_2O, CO_2, O_2, and SO_2) evolve from volatile-bearing phases (e.g., minerals and organics) at characteristic temperatures were used to identify the presence of organic or particular mineral phases. The SAM plumbing is configured to allow the MS to sample a portion of evolved gases over the entire sample heating range. After the evolved gas were sample by the MS, gases flowed downstream and were then either sampled by the hydrocarbon trap for GCMS analysis or the TLS or exhausted to the Martian atmosphere.

Hydrocarbon detections using GCMS and isotopic analysis of water and CO_2 using the TLS are discussed elsewhere [*Glavin et al.*, 2013; *Leshin et al.*, 2013; *Ming et al.*, 2014; *Freissinet et al.*, 2015; *Mahaffy et al.*, 2015]. This work focuses on evaluation of H_2O (m/z 20), H_2 (m/z 2), SO_2 (m/z 64), H_2S (m/z 34) CO_2 (m/z 44), CO (m/z 28), NO (m/z 30), O_2 (m/z 32), and HCl (m/z 36) evolved gases as analyzed by only the direct MS pathway and is referred to as the SAM-EGA mode. The isotopologue of water, m/z 20, is presented instead of the m/z 18 signal, which was saturated on every analysis because of the extreme sensitivity of the MS. Procedures and methods utilized for quantifying total evolved gas releases (e.g., μmol or nmol) and their associated errors are described in detail elsewhere [*Archer et al.*, 2014]. Evolved gas totals were then used with estimated sample mass deliveries to SAM to calculate evolved gas contents (e.g., wt % or μg/g). Evolved gas content errors are based on propagation of errors derived from sample mass delivery and evolved gas totals.

2.2. SAM-EGA Signal Processing

All evolved gas plots were deadtime and background corrected, while many of the evolved gas plots were further processed to account for MS signal saturation and/or the presence of isotopologue fragments created in the MS. Deadtime correction refers to a process that accounts for lost counts during high count rates. Detailed description of deadtime correction procedure was outlined by *Franz et al.* [2014]. The SAM-EGA analysis of calcite ($CaCO_3$) and melanterite ($FeSO_4 \cdot 7H_2O$) standards using the SAM instrument before integration into the rover allowed for correction factors to be derived that were applied to m/z 28, m/z 32, m/z 34, m/z 44, and m/z 64. These two standards in several cases were used as proxies for the isotopic ratios in the signal-saturated Mars samples that were attributed to CO_2 and SO_2 evolving phases that differed from the CO_2 and SO_2 evolving standard phases. This could provide inaccurate isotopic measurements which is not necessarily critical when correcting figures for presentation purposes but is important when reporting evolved gas abundances discussed in this work. Derivation of error associated evolved gas abundance determinations as a result of using these two standards is beyond the scope of this work and can be found elsewhere [*Archer et al.*, 2014].

Many samples experienced signal loss of the most intense portions of the m/z 44 (CO_2) and m/z 64 (SO_2) peaks as a result of signal saturation of the MS detector. The missing portions of these peaks were replaced by corrected isotopologue m/z 45 (CO_2) and m/z 66 (SO_2) plots, respectively. The missing portions of the m/z 44 signal was replaced by a correction to the m/z 45 plot from the Gale sample based on m/z 44//m/z 45 ratio calculated from the calcite standard. Subscripts *c* and *uc* indicate corrected and uncorrected

SAM-EGA plots of Gale samples, respectively, and mineral subscript refers to mineral standard analyzed in SAM before flight.

$$m/z\ 44_c = m/z\ 45_{Gale} \bullet (m/z\ 44//m/z\ 45)_{calcite}.$$

Similar to m/z 44, when m/z 64 was saturated, the missing portion of the m/z 64 peak was derived from m/z 66:

$$m/z\ 64_c = m/z\ 66_{Gale} \bullet (m/z\ 64//m/z\ 66)_{melanterite}.$$

Signal loss was not always complete for m/z 44 or m/z 64 plots, and only the missing (i.e., saturated signal) portions of the m/z 44 or m/z 64 peaks were replaced with corrections from m/z 45 and m/z 66, respectively.

The m/z 28 signal was composed of evolved CO from the sample and the CO isotopologue fragment of CO_2 created in the MS during analyses. The CO isotopologue fragment contribution was based on m/z 28//m/z 44 ratio calculated from calcite standard run in SAM where no CO producing phase was present. The CO isotopologue fragment contribution was subtracted from the uncorrected m/s 28_{uc} plot to obtain the corrected m/s 28_c plot:

$$m/z\ 28_c = m/z\ 28_{uc} - m/z\ 44_c \bullet (m/z\ 28//m/z\ 44)_{calcite}.$$

All low-temperature (<500°C) m/z 32 was assumed to be derived from oxychlorine thermal decomposition as there were no significant SO_2 (m/z 64) detections at those temperatures. All m/z 32 detections above 500°C had contributions from SO_2 (^{32}S) that were subtracted out using m/z 32//m/z 64 ratio determined from the melanterite standard.

$$m/z\ 32_c = m/z\ 32_{uc} - m/z\ 64_c \bullet (m/z\ 32//m/z\ 64)_{melanterite}.$$

The O_2 ($^{18}O^{16}O$) and SO_2 (^{34}S) isotopologue fragments must be subtracted from m/z 34 to acquire m/z 34 due to H_2S. The presence of high concentration of oxychlorine phase indicated that O_2 was contributing to all low-temperature (<500°C) m/z 34 and that if H_2S was present below 500°C it would be difficult to distinguish it from $^{18}O^{16}O$ from oxychlorine. The m/z 34 peak that coincided with O_2 below 500°C in the Gale sample was used to calculate m/z 34//m/z 32 ratio of the Gale sample. Contributions to m/z 34 from SO_2 (^{34}S) were also subtracted from the m/z 34 plot using the m/z 34//m/z 64 ratio calculated from the melanterite standard.

$$m/z\ 34_c = m/z\ 34_{uc} - \left[m/z\ 32_c \bullet (m/z\ 34//m/z\ 32_c)_{Gale}\right] - \left[m/z\ 64_c \bullet (m/z\ \ 34//m/z\ \ 64)_{melanterite}\right].$$

2.3. MTBSTFA Contributions to CO_2 and NO Detections

The derivatization agent, N-methyl-N-(*tert*-butyldimethylsilyl)trifluoroacetamide) (MTBSTFA), that was brought for wet chemistry SAM-GCMS analysis was determined to have leaked from one of the sealed cups in SAM and likely contributed to SAM-EGA detections of CO_2 and NO [*Glavin et al*., 2013; *Freissinet et al*., 2015; *Stern et al*., 2015]. The worst-case scenario contributions of MTBSTFA-C to SAM-CO_2 detections were proposed to be 900 nmol C for each SAM-EGA analysis [*Glavin et al*., 2013]. The detection of MTBSTFA breakdown byproducts used to estimate the level of MTBSTFA that leaked into SAM indicates that MTBSTFA did not undergo complete combustion to CO_2 and thus could cause this estimate to be lower [*Glavin et al*., 2013]. Nevertheless, 900 nmol CO_2-C from MTBSTFA for each analysis whether it was a single or triple portion was used as worst-case scenario when discussing CO_2-C contents. The impact this level of MTBSTFA-CO_2 has on total CO_2 contents will be discussed in section 4.6.

The MTBSTFA contribution to the NO detected by SAM-EGA was determined by the background correction method by *Stern et al.* [2015]. Briefly, MTBSTFA decomposes into nitrogen-free ion fragments that were detected by SAM-EGA which include tert-butyldimethylsilanol (monosilylated H_2O, MSW) (m/z 75), 1,3-bis(1,1-dimethylethyl)-1,1,3,3-tetramethyldisiloxane (bisilylated H_2O, BSW) (m/z 147), tert-butyldimethylfluorosilane (TBDMS-F) (m/z 134), 2-methylpropene (C_4H_8) (m/z 41), and a strong contribution at m/z 15, either CH_4 or methylene ions ([*Stern et al*., 2015], supporting information). The detection of these fragment masses in the sample of interest indicates how much MTBSTFA decomposed. Each MTBSTFA

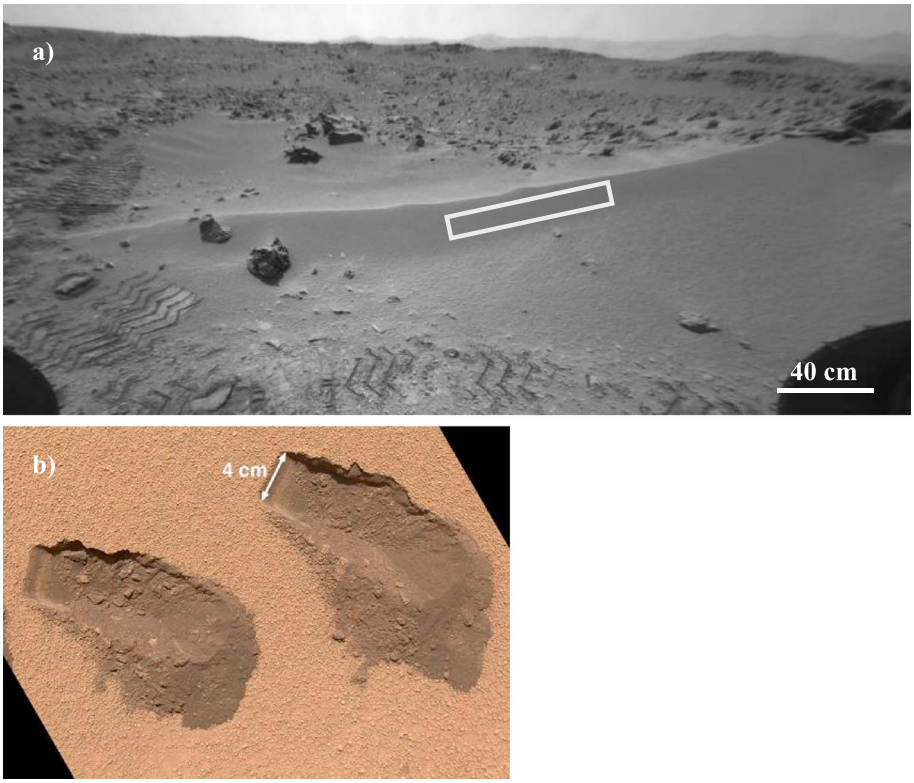

Figure 3. (a) The Rocknest eolian drift before sampling (Front Hazcam-FLA_402468252ILTLF0043474FHAZ00308M1, sol 56). White rectangle indicates approximate location of where the five scoops were acquired. Individual wheel tracks are 40 cm wide. (b) Rocknest scoops 3 and 4 (MAHLI-0084MH0001120010100946E01, sol 84).

molecule has 1 nitrogen, and thus, the amount of nitrogen presumably evolved as NO when MTBTSFA decomposed can be calculated as follows:

$$\mathrm{MTBSTFA-nitrogen} = 2\mathrm{xBSW} + \mathrm{MSW} + \mathrm{TBDMS} - \mathrm{F} + \mathrm{C_4H_8} + 1/5\mathrm{xCH_4}$$
$$\mathrm{Corrected-nitrogen} = \mathrm{Total\ nitorgen\ detected\ by\ SAM} - \mathrm{EGA} - \mathrm{MTBSTFA-nitrogen}.$$

2.4. O_2 Corrections From Nitrate Decomposition.

Evolved oxygen used to calculate the amount of oxychlorine present must account for contributions from nitrate thermal decomposition which also evolved O_2 [e.g., *Ettarh and Galwey*, 1996]. For example,

$$2\mathrm{Ca(NO_3)_2} \rightarrow 2\mathrm{CaO} + 4\mathrm{NO} + 3\mathrm{O_2}. \quad (1)$$

Oxygen contribution from nitrate was calculated by multiplying MTBSTFA-corrected nitrate amount by 0.75 and subsequently subtracting this nitrate oxygen from total oxygen evolved at temperatures consistent with oxychlorine thermal decomposition. Evolved oxygen above 600°C from sulfate decomposition were not corrected for nitrate oxygen as these temperatures were too high to have contributions from nitrate thermal decomposition. The relatively low amounts of Gale nitrate resulted in between 1 and 8% of the evolved O_2 to be attributed to nitrate thermal decomposition.

2.5. Sampling Procedures

Eleven sampling sites as of sol 1237 (29 January 2016) have been examined by SAM. One sample was scooped from an eolian drift deposit dubbed Rocknest (RN), while two eolian dune samples of differing particle size distributions were scooped from Gobabeb (GB1 and GB2) (Figures 3 and 4). The other nine samples were acquired from sedimentary rocks using a drill and are listed in order of acquisition: John Klein (JK), Cumberland (CB), Windjana (WJ), Confidence Hills (CH), Mojave 2 (MJ), Telegraph Peak (TP), Buckskin (BK), Big Sky (BS), and Greenhorn (GH) (Figures 5–9). The RN, JK, CB, WJ, and CH samples included a blank

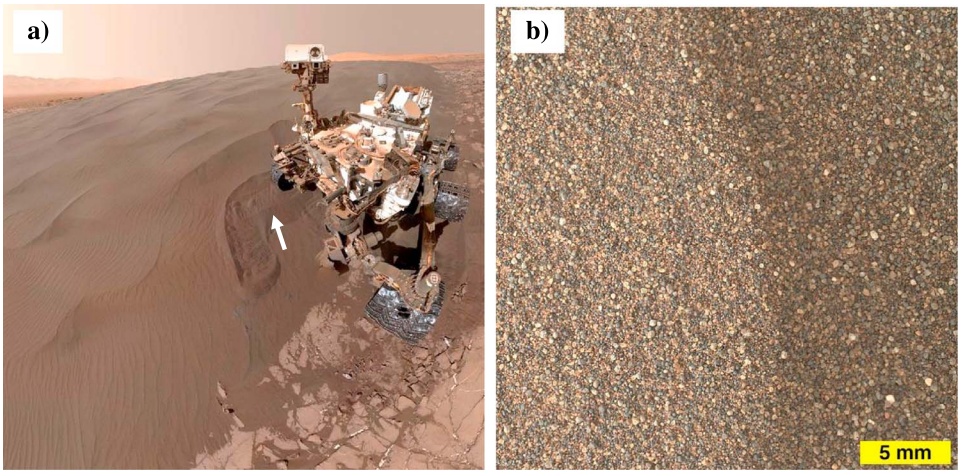

Figure 4. (a) Curiosity rover, for scale, at the Gobabeb sample extraction site on the north side of the active eolian Namib Dune sand dune in the Bagnold dune field. This is a radiometrically corrected, color-adjusted mosaic of MAHLI images acquired on sol 1228. White arrow points to location of scoop 1 (NASA/JPL-Caltech/MSSS product PIA20316). (b) Gobabeb Scoop 1 site before the sample was extracted. Illuminated by sunlight from the left, an eolian sand ripple crest runs up the center of this figure, a portion of MAHLI focus merge product 1224MH0001700000403204R00 created on board the instrument from eight focus stack images acquired on sol 1223.

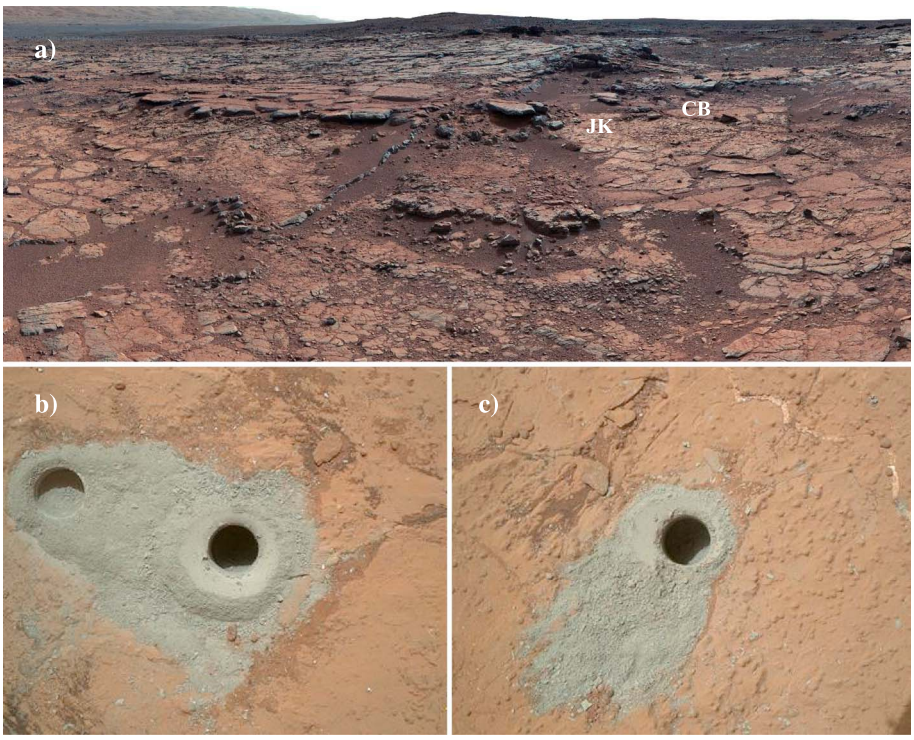

Figure 5. (a) The John Klein (JK) and Cumberland (CB) sampling sites in the Sheepbed member of Yellowknife Bay formation with view to the southwest (Mastcam-34 white balanced mosaic mosaic from sequence mcam00818, sol 137). JK and CB are ~2.75 m apart. (b) The JK sample extraction drill hole (center) created on sol 182 with shallower hole (left) that was drilled on sol 180 to interrogate the rock properties before commitment to drill a full-depth hole (Portion of MAHLI image 0182MH0002300010102629C00) (c) The CB sample extraction drill hole created on sol 279 (Portion of MAHLI image 0279MH0002680020103055C00). Drill holes are ~1.6 cm wide.

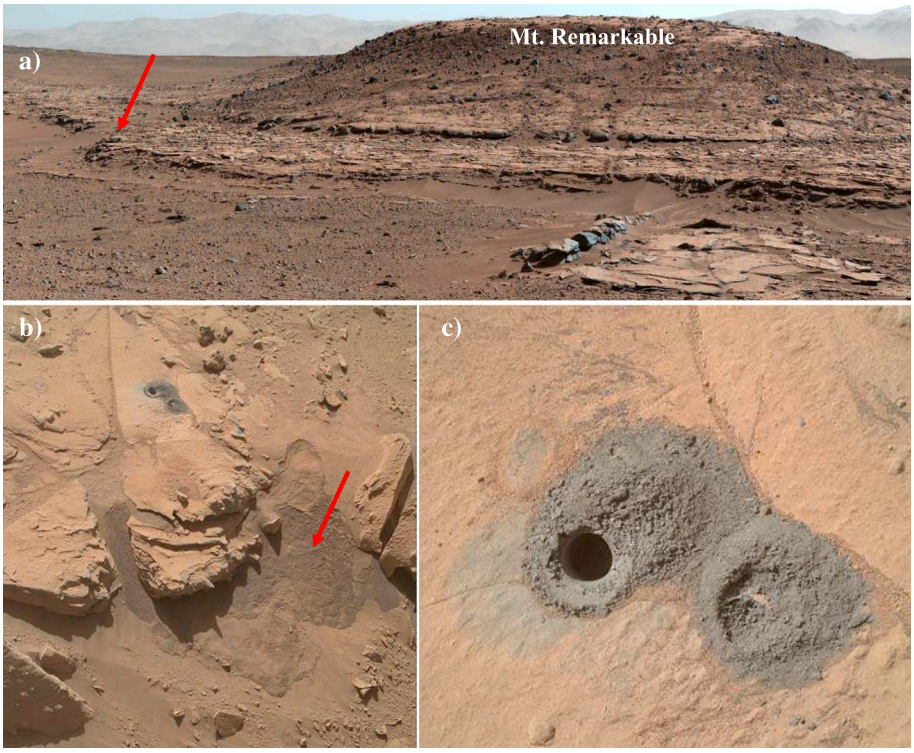

Figure 6. (a) Context of the Windjana (WJ) sample extraction site (arrow) in the Dillinger member of the Kimberley formation, located at the base of the ~4 m high Mount Remarkable. The west-northwest wall of Gale Crater is visible in the distant background (Mastcam-100 white balanced mosaic from sequence mcam02509, sol 595). (b) Local context of the WJ drill hole in Dillinger member sandstone as viewed by MAHLI (image 0627MH0003900000203473E01, sol 627). Drill activity caused local slumping of windblown sand (arrow) that had been accumulated against the outcrop. (c) The WJ drill hole (drilled on sol 621; left) and preceding shallow interrogation hole (drilled on sol 615, right). This is a portion of a mosaic of sol 627 MAHLI images 0627MH0001900010203476C00, 0627MH0001900010203478C00, and 0627MH0003970010203510C00. Drill holes are 1.6 cm wide.

SAM-EGA analysis of an empty cup prior to the sample run. Only the H_2 blank analysis for RN is not reported as this mass (m/z 2) nor its isotopologue (m/z 3) was analyzed by SAM. The GH blank analysis was conducted between the GH1 and GH2 analyses. The cup used for each blank analysis was always used for the subsequent sample analysis by SAM. All drilled samples were acquired with a drill that produced a 1.6 cm diameter by ~6 to 6.5 cm deep hole. The drill design causes the top 1.5 cm of drilled material to not be included in the sample and is instead extruded as cuttings onto the adjacent rock surface [*Anderson et al.*, 2012]. The extruded cuttings are referred to as drill tailings. All samples except one were passed through a 150 μm sieve in the rover's sample processing and handling system, which has the capability of delivering small sample portions to the analytical instruments [*Anderson et al.*, 2012]. The exception is the GB2 sample which consisted of a scooped 150 μm to 1 mm fraction. The scooped RN sample was a single portion amounting to 50 mg ± 8 (2σ) whereas the drilled single portion samples of JK, CB, CH, MJ, and TP amounted to 45 mg ± 18 (2σ). Triple portions [135 mg ± 31(2σ)] of drilled WJ, BK, BS, GH, and scooped GB1 were delivered to enhance organic detection. The amount of scooped coarser grained (150 μm to 1 mm) GB2 sample delivered to SAM was unknown because sample delivery models used to calculate delivery amount were based on finer grained components (<150 μm) and sample delivery models for the coarse-grained components have yet to be developed.

Eight samples were only analyzed once but four samples (RN, JK, CB, and GH) analyzed multiple times to collect TLS and GCMS data over different temperature ranges and expose samples to prerun heat treatments to minimize low-temperature background organic detections (Table 1) [e.g., *Leshin et al.*, 2013; *Freissinet et al.*, 2015]. The SAM EGA results from all the RN subsamples are similar, and thus, the RN subsample 4 profile was presented for brevity. Four and seven subsamples of the JK and CB drilled material,

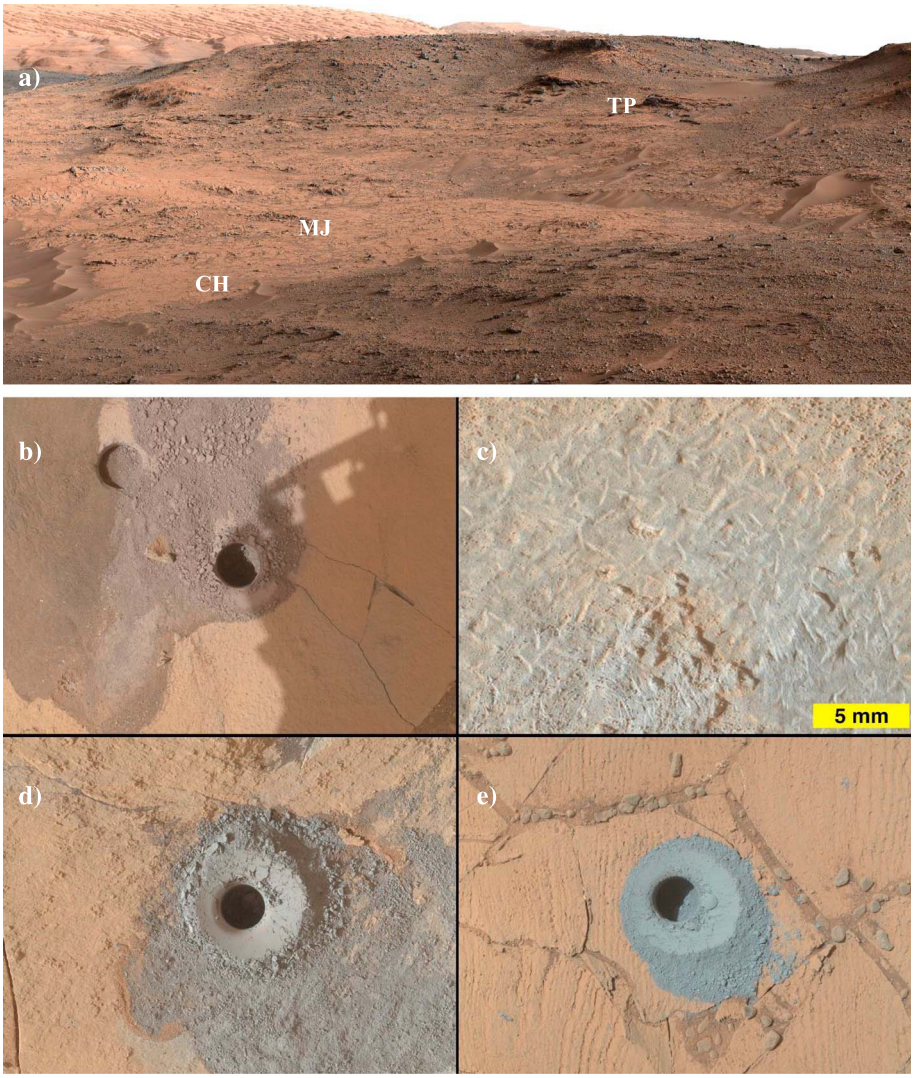

Figure 7. (a) The Pahrump Hills member sampling site for Confidence Hills (CH), Mojave 2 (MJ), and Telegraph Peak (TP). MJ is 10 m from and 1 m above CH, while TP is ~6 m above and ~39 m from MJ (A portion of the Mastcam-34 white balanced mosaic from sequence mcam03229, sol 751). (b) The CH drill hole (center), created on on sol 759, and preceding shallow rock properties interrogation hole (top left), drilled on sol 756; (MAHLI image 0759MH0003970010300030C00, sol 759). (c) Brushed MJ material showing crystal forms of lenticular morphology of about 1–2 mm length (MAHLI focus merge product 0880MH0004620000302350R00, sol 880). (d) The MJ drill hole created on sol 882 (MAHLI- 0882MH0003970010302481C00, sol 882). (e) The TP drill hole created on sol 908 (MAHLI-0908MH0003970010302871C00, sol 908). Drill hole diameters are ~1.6 cm.

respectively, were analyzed by SAM. Despite preconditioning all sample cups before analyses to 870°C, select JK and CB subsamples underwent additional heat treatments to minimize organic background levels [*Ming et al.*, 2014; *Freissinet et al.*, 2015]. The JK1, JK2, and JK3, subsamples underwent heat treatments to 320°C. The CB5, CB6, and CB7 empty cups were heated to 250°C allowed to cool. The CB6 and CB7 subsamples were loaded into the cups and heated again to 250°C for 27 min for before continuing the heating to 870°C (Table 1). The CB6 and CB7 subsamples are not presented because heating to these temperatures were shown to affect SAM H_2O, CO_2, CO, and O_2 low-temperature evolutions. The CB1, CB2, and CB3 were analyzed similarly without cup reheating or sample preheating. Several CB1 evolved gas abundances were much less than CB2, CB3, and CB5 which may have been attributed to less sample being dumped into the cup relative to the other subsamples; thus this subsample will not be discussed. The evolved gas release profiles for CB2, CB3, and CB5 are similar [*Ming*

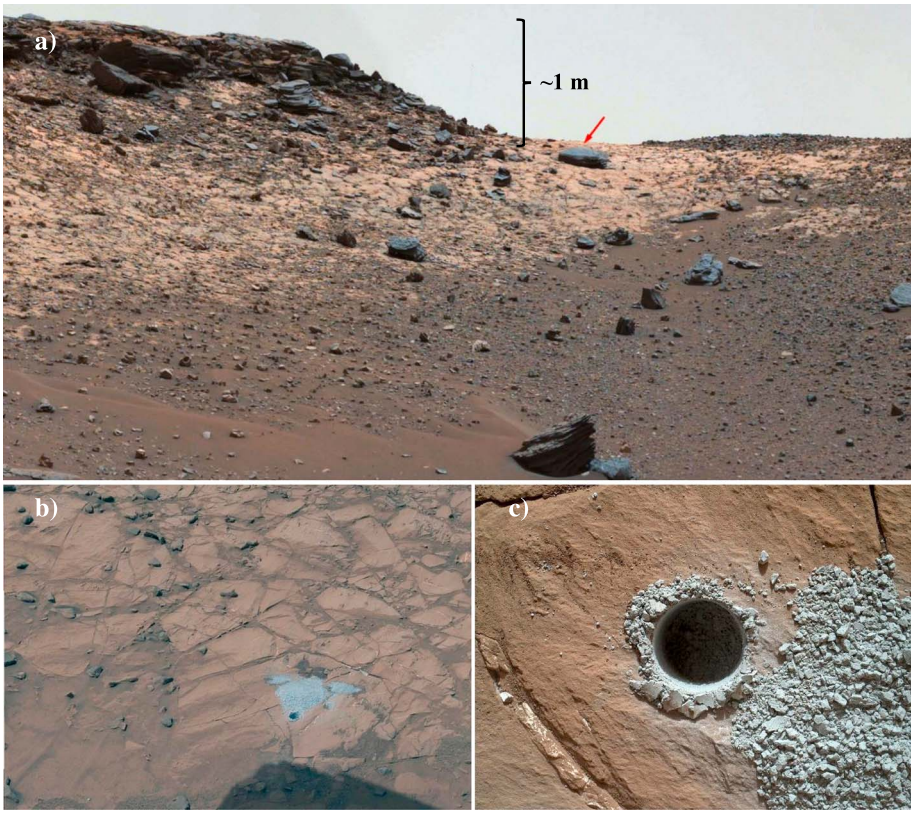

Figure 8. (a) The Buckskin sampling site of the Murray formation in the Marias Pass region. Red arrow marks approximate BK acquisition location behind rock. Sampling location to plateau top at top left is ~1 m (Portion of a Mastcam-34 white balanced mosaic from sequence mcam04375, sol 990). (b) The geological surroundings of the BK drill hole (Portion of Mastcam-34 white balanced image 1062ML0046720020306187E01, sol 1062). (c) The BK drill hole (Portion of MAHLI image-1060MH0003970010400402C00, sol 1060). Drill hole diameter is ~1.6 cm.

et al., 2014]; thus, only CB2 profiles are presented. JK4 is presented in this work as it is the only JK subsample to not have undergone any preheating before SAM-EGA analysis. Two GH subsamples were analyzed because the evolved gases from overlapping temperature ranges were examined by TLS and GCMS in GH1 and GH2, respectively. Furthermore, the GH1 subsample was deposited over the residue of the previously analyzed BS sample in the same cup, while the GH2 subsample was placed in an empty cup. The GH1 and GH2 have similar profile releases for most gases though there are some differences in release temperatures between the two samples. The reasons for the differences in temperature of gas releases between the two samples is not clear and may be attributed to GH1 and BS residue sample interaction. The GH2 analysis is presented to maintain consistency with other samples that were analyzed in unused cups.

2.6. Alpha-Particle X-Ray Spectrometer Sample Analysis

Aliquots of all samples analyzed by SAM were also analyzed by Alpha-Particle X-ray Spectrometer (APXS) for total chemistry; however, only total sulfur and total chlorine are presented, because these are the only elements that can be directly compared to SAM data, namely, evolved SO_2 and HCl, respectively. Details of the APXS method, the instrument, and operation are explained elsewhere [*Gellert et al*., 2006, 2015; *Campbell et al*., 2012; *Schmidt et al*., 2014; *Berger et al*., 2016; *Thompson et al*., 2016a]. Briefly, the scooped or drilled material was acquired by the rover's sample acquisition, processing, and handling (SA/SPaH) system which then passed portions of the sample through a sieve to CheMin and SAM for analysis [*Anderson et al*., 2012]. The remaining sieved material of each sample was then dumped onto the Martian surface at a later date and subsequently analyzed by APXS. The sieved material was dumped in an amount that exceeded the APXS field of view which avoided analyzing chemistry of the underlying material. This "postsieve" sample APXS analysis was then compared to the SAM data (supporting

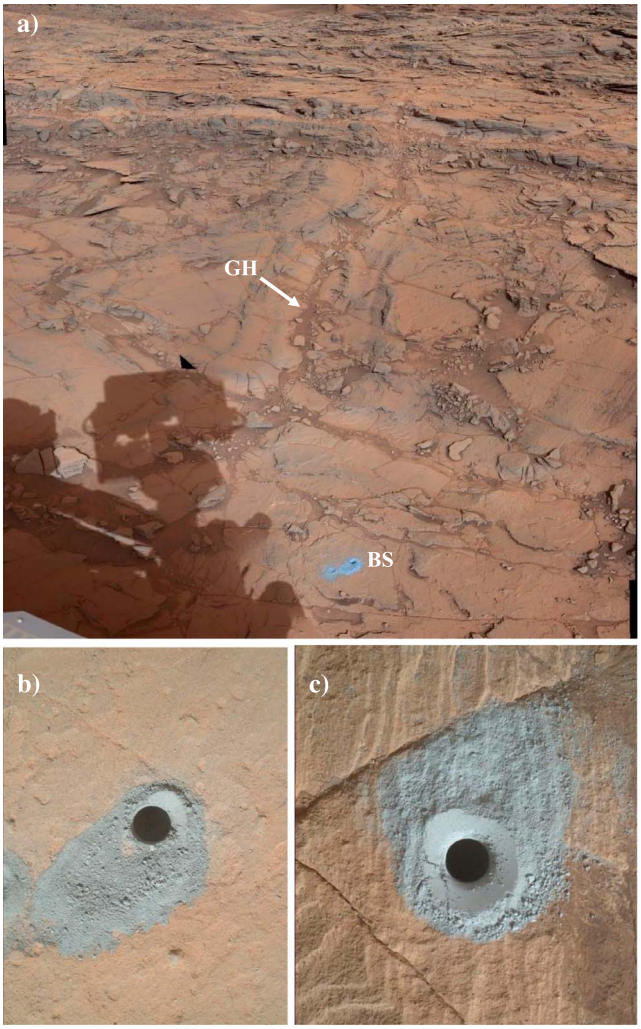

Figure 9. (a) Sample extraction site at fracture-associated halo in Stimson formation eolian sandstone at Big Sky (BS) and Greenhorn (GH). BS occurs outside of halo, while GH occurs within halo (white balanced Mastcam mosaic, sol 1112–1126; NASA/JPL Photojournal web release PIA-20270. (b) Big Sky drill hole (MAHLI-1119MH0003970010401458C00, sol 1119). (c) The GH drill hole (MAHLI-1137MH0003970010401960C00, sol 1137). Drill hole diameters are 1.6 cm.

information Tables S3 and S9). Mars Hand Lens Imager (MAHLI) images of the postsieve dump sample were acquired to verify adequate coverage of underlying surface. Furthermore, APXS analyses of sample drill tailings not acquired by the SA/SPaH and presieve sample acquired by SA/SPaH were used to assess if the postsieve APXS analysis was successfully taken and if it represented the best APXS data set for comparison with SAM.

The APXS determines the composition of the sample using X-ray spectroscopy by excitation with high energetic alpha-particles and X-rays from the internal 244Cm sources. The method resembles a combination of the terrestrial standard methods of particle induced X-ray emission and X-ray fluorescence. Sulfur and chlorine are unambiguously identified by their characteristic X-ray energy and quantified with small statistical uncertainty down to a few 1000 ppm abundance. The signal for these two elements stems from about 5 to 10 μm within the sample. The Cl and S accuracy determined during calibration was 30% and 15% absolute APXS error, respectively. The underlying reason for the accuracy errors is that the APXS calibration assumes a homogeneous sample for the correction of self-absorption within the sample. The Cl and S unfortunately occur within heterogeneous natural samples that can cause absorption effects of the S and Cl X-ray signal which can skew abundance determinations.

2.7. Image Processing for Figures

The images (Figures 1 and 3–9) used in this report to document Curiosity's sample extraction sites were acquired by the Mars Reconnaissance Orbiter (MRO) High Resolution Imaging Experiment (HiRISE) camera [*McEwen et al.*, 2007], the MSL Mast Cameras (Mastcams) [*Malin et al.*, 2010], the MSL robotic arm-mounted Mars Hand Lens Imager (MAHLI) [*Edgett et al.*, 2012], and the MSL front Hazard cameras (Hazcams) [*Maki et al.*, 2012]. The figures include cropped portions of singular Mastcam, MAHLI, and Hazcam images; cropped portions of mosaics consist of multiple Mastcam, MAHLI, and HiRISE images; and MAHLI focus merge products created on board the instrument. The images have been processed to enhance the visibility of the key illustration details via broadening image dynamic range and contrast sharpening. Some of the images and mosaics, as indicated in figure captions, have been radiometrically corrected and white balanced. White balanced color shows what the geologic materials would look like if they were in sunlight on Earth; this processing can sometimes cause the sky to appear blue or white. Other images retain their natural color as they appear under Martian illumination conditions.

Table 1. Samples Analyzed by SAM[a]

Sample	Sample Mass	Scooped (S) Drilled (D) Sol	SAM Analysis Sol	Cup/Sample Pretreatment Temperatures (°C)	Sample Heating Temperatures (°C)
RN Blank 1	0	-	86	None	40–870
RN Blank 2	**0**	**-**	**88**	**None**	**40–870**
RN1	50 ± 8	S-93	93	None	40–870
RN2	50 ± 8	S-93	96	None	40–870
RN3	50 ± 8	S-93	99	None	40–870
RN4	**50 ± 8**	**S-93**	**117**	**None**	**40–870**
JK Blank	0	-	177	Cup 320	320–870
JK1	45 ± 18	D-180	196	Sample 320	320–870
JK2	45 ± 18	D-180	198	Sample 320	320–870
JK3	135 ± 31	D-180	224	Sample 320	320–870
JK4	**45 ± 18**	**D-180**	**227**	**None**	**40–870**
CB Blank 1	**0**	**-**		**None**	**40–870**
CB1	45 ± 18	D-279	282/283	None	40–870
CB2	**45 ± 18**	**D-279**	**286**	**None**	**40–870**
CB3	45 ± 18	D-279	290	None	40–870
CB5	45 ± 18	D-279	368	Cup 200	40–870
CB6	135 ± 31	D-279	382	Cup 250 Sample 250	250–870
CB6 reheat	135 ± 31	D-279	394	Cup 250 Sample 250	250–870
CB7	135 ± 31	D-279	408	Cup 250 Sample 250	250–870
CB Blank 2	0	-	421	Cup 250 Sample 250	250–870
WJ Blank	**0**	**-**	**602**	**None**	**40–870**
WJ	**135 ± 31**	**D-621**	**624**	**None**	**40–870**
CH Blank	**0**	**-**	**770**	**None**	**40–870**
CH	**45 ± 18**	**D-759**	**773**	**None**	**40–870**
MJ	**45 ± 18**	**D-881**	**887**	**None**	**40–870**
TP	**45 ± 18**	**D-908**	**928**	**None**	**40–870**
BK	**135 ± 31**	**D-1060**	**1076**	**None**	**40–870**
BS	**135 ± 31**	**D-1120**	**1130**	**None**	**40–870**
GH1	135 ± 31	D-1137	1147	None	**40–870**
GH Blank	**0**	**-**	**1171**	**None**	**40–870**
GH2	**135 ± 31**	**D-1137**	**1178**	**None**	**40–870**
GB1	**135 ± 31**	**S-1224**	**1224**	**None**	**40–870**
GB2	**unknown**	**S-1224**	**1237**	**None**	**40–870**

[a]Bold samples are presented in this work. See text for descriptions of sample and cup pretreatment procedures.

3. Geologic Context

3.1. Eolian Sediment Samples Analyzed by SAM

3.1.1. Rocknest

The Curiosity rover landed in northern Gale Crater on Aeolis Palus on an exposure of the Bradbury group fluvial conglomerate rocks which are the oldest strata exposed in this part of Gale Crater (Figure 1) [*Williams et al*., 2013; *Vasavada et al*., 2014]. The Bradbury group underlies the Mount Sharp group and is exposed in the crater plains along the north side of Mount Sharp (Figure 2). The Curiosity rover drove 400 m east-southeast of the landing site to the first SAM sampling stop at the RN eolian drift material (−4518 m elevation). Sediments from the RN eolian drift deposit were sampled in five different locations within the deposit (Figure 3) but only scoop five sampled on sol 93 was examined by SAM. The Rocknest material consists of unconsolidated sand and dust [*Blake et al*., 2013; *Minitti et al*., 2013] that overlies rock of the Glenelg member of the Yellowknife Bay formation (Figure 3). The RN material likely consists of a mixture of local, regional, and global sources that yield a bulk basaltic chemistry that is similar to eolian material at other landing sites [*Blake et al*., 2013; *Minitti et al*., 2013].

The bulk Rocknest sediment possesses a basaltic mineralogy consisting of plagioclase feldspar, olivine, pyroxenes, ilmenite and magnetite and a secondary mineralogy that includes calcium sulfates and hematite [*Bish et al*., 2013; *Blake et al*., 2013]. A broad hump in the X-ray diffraction pattern is consistent with the

presence of X-ray amorphous material that may consist of basaltic glass, allophane (e.g., hisingerite) poorly crystalline sulfate, and/or nanophase Fe oxides (e.g., ferrihydrite) [*Bish et al*., 2013].

3.1.2. Gobabeb 1 and 2

The Gobabeb sand samples were scooped from the lower stoss slope of a dune informally named Namib Dune which is part of the active informally named Bagnold Dune Field (Figure 4) [*Silvestro et al*., 2013]. The Gobabeb sediment unconformably overlies Murray formation mudstone (−4424 m). Examination of the sieved <150 μm fraction of the sediment indicates the GB1 samples contains grains that are mostly resolvable by MAHLI (Figure 4b). The <150 μm RN material by comparison contains at least 40% material that is unresolvable by MAHLI [*Minitti et al*., 2013]. The overall total chemistry of the GB samples is similar to RN except that the GB has a lower S/Cl ratio than RN [*Ehlmann et al*., 2017]. The overall mineralogical abundance of GB is similar to RN and consists of plagioclase feldspar, olivine, augite, pigeonite, and magnetite [*Achilles et al*., 2017].

3.2. Bedrock Samples Analyzed by SAM

3.2.1. John Klein and Cumberland (Bradbury Group-Yellowknife Bay Formation-Sheepbed Member-Mudstone)

The JK and CB sampling sites in the Sheepbed mudstone occur near the topographically and stratigraphically lowest point along the MSL rover traverse (~−4520 m) [*Grotzinger et al*., 2014, 2015] and are located ~444 m east of the Bradbury landing site and ~100 m northeast of RN (Figures 1, 2, and 5). The JK and CB samples were drilled (sols 180 and 279, respectively) and extracted from the Sheepbed lacustrine mudstone. The two samples are separated by 2.75 m and 10 cm, horizontally and vertically, respectively [*Ming et al*., 2014] (Figure 5a).

The JK and CB materials possess a basaltic mineralogy similar to RN along with calcium sulfate, iron oxide/hydroxides, and high X-ray amorphous content (28–31 wt %) that consists mostly of Si, Fe, Ca, and S [*Vaniman et al*., 2014]. The JK drill hole wall showed light-toned millimeter-sized veins that were high in Ca, S, and H, which was determined to be consistent with bassanite [*Rapin et al*., 2016]. The CB drill hole wall had far fewer veins than JK [*Vaniman et al*., 2014]. Unlike RN, iron sulfides and smectite (saponite) were detected in these samples. The presence of smectite and magnetite along with the low abundance of olivine in JK and CB relative to RN suggests that these secondary phases formed under near neutral pH conditions in the Sheepbed mudstone [*McLennan et al*., 2014; *Vaniman et al*., 2014; *Bristow et al*., 2015]. Both of these drilled materials are grey in color highlighting the reduced nature of these materials (Figures 5b and 5c) [*Ming et al*., 2014].

3.2.2. Windjana (Bradbury Group-Kimberley Formation-Dillinger Member-Sandstone)

The Windjana (WJ) drilled sample was extracted from a sandstone outcrop that occurs ~4 km southwest and ~40 m stratigraphically higher than the Sheepbed mudstone samples (CB and JK) (Figures 1 and 2). The WJ sample was acquired (sol 621) from the Dillinger member of the Kimberley formation that is dominated by fluvial conglomerate and deltaic sandstone (Figure 6) [*Treiman et al*., 2016]. The Windjana material consists of a crossstratified sandstone of likely eolain origin that reflects reworking of fluvial sand [*Grotzinger et al*., 2015; *Treiman et al*., 2016]. The WJ sample has a potassium-rich basaltic mineralogy as indicated by the high concentration of K-feldspar (~22 wt %) [*Thompson et al*., 2016a; *Treiman et al*., 2016]. This potassium-rich feldspar mixed with basaltic minerals indicates that the WJ material is derived from multiple parent rock sources. The Windjana sample also possesses high pyroxene and magnetite contents along with a 2:1 layer type phyllosilicate and X-ray amorphous material [*Downs and MSL Science Team*, 2015; *Treiman et al*., 2016]. Postdepositional diagenetic processes are likely responsible for cementing the WJ with magnetite, 2:1 layer type phyllosilicate, and Fe-rich X-ray amorphous material of ferrihydrite composition [*Treiman et al*., 2016].

3.2.3. Confidence Hills, Mojave, and Telegraph Peak (Mount Sharp Group-Murray Formation-Pahrump Hills Outcrop-Mudstone)

The CH, MJ, and TP materials were the first drilled (sols 759, 881, 908, respectively) samples of the Murray formation (basal layer of the Mount Sharp group) (Figure 7). The Murray formation forms an interfingering contact with the Bradbury group (Figure 2), and the samples are located ~2.2 km to the southwest of WJ and ~20 m higher stratigraphically [*Stack et al*., 2015; *Grotzinger et al*., 2015] (Figures 1 and 2). The Murray formation is dominated by finely laminated mudstones interpreted to have been deposited in a lacustrine environment in the proximity of a fluvial-deltaic depositional setting [*Grotzinger et al*., 2015]. The CH site (−4461 m) is approximately 1 m stratigraphically below and 10 m from MJ (−4459 m), while TP (−4453)

is 6 m stratigraphically above and ~39 m to the south of MJ (Figures 2 and 7a). Diagenetic features (crystal clusters/dendrites) high in Mg, S, and Ni occur near CH and MJ [*Gellert et al*., 2015; *Thompson et al*., 2015; *Grotzinger et al*., 2015; *Kah et al*., 2015; *VanBommel et al*., 2016; *Nachon et al*., 2017]. The CH and MJ samples were drilled from locations without crystal clusters, dendrites veins, or nodules. The MJ sample was acquired because it possessed bright crystal forms with lenticular morphology [*McBride et al*., 2015] (Figure 7c); which were not present in CH. Telegraph Peak was analyzed because it had higher Si and lower Mg contents than CH and MJ.

The Pahrump Hills mineralogy as determined by CheMin suggested a complex geochemical history where minerals stable under acidic (jarosite), alkaline (apatite), oxidizing (sulfate), and reducing (magnetite) conditions are present [*Rampe et al*., 2017]. Confidence Hills has the highest hematite concentration of all samples reported here, and this was demonstrated by CH having the reddest coloration of any of the drilled sediments (Figure 7b). The presence of jarosite and high hematite contents in CH and MJ suggests that these materials may have been exposed to acidic-oxidizing conditions after deposition. Greater magnetite contents in TP, however, suggested that more reducing conditions may have prevailed in TP. Furthermore, the occurrence of apatite in CH, MJ, and TP, which is not stable under acidic pH conditions, is difficult to reconcile suggesting again that Gale Crater sediments possess a complex geochemical history. TP also contained abundant cristobalite, marking the first detection of crystalline silica in the mission. The Pahrump Hills materials possessed a high X-ray amorphous concentration (up to 53 wt %). A 2:1 layer type phyllosilicate was also detected, but similar to WJ, the phyllosilicate concentrations were lower than what was detected in JK and CB [*Rampe et al*., 2017].

3.2.4. Buckskin (Mount Sharp Group-Murray Formation-Marias Pass Outcrop-Mudstone)

The BK sample was drilled (sol 1060) in the Murray formation about 6 m stratagraphically above and ~600 m to the southwest of TP, in the Marias Pass outcrop (Figures 1, 2, and 8). The BK sample came from a finely laminated mudstone [*Morris et al*., 2016]. The BK sample was drilled because it exhibited high Si (73.7 wt % SiO_2) and Ti (1.6 wt % TiO_2) contents [*Morris et al*., 2016]. The Buckskin mudstone contains abundant SiO_2-enriched X-ray amorphous material (~60 wt %) and has no detectable phyllosilicates [*Morris et al*., 2016]. Other phases present include tridymite (~14 wt %), a high-temperature SiO_2 polymorph, magnetite, minor cristobalite, and anhydrite [*Morris et al*., 2016]. Much of the silica polymorphs in the Marias Pass region are likely detrital from a silicic source region [*Morris et al*., 2016], although some of the amorphous silica could have resulted from postdepositional acidic weathering of the Buckskin materials, causing passive enrichment in Si and Ti [*Morris et al*., 2016; *Rampe et al*., 2017; *Schmidt et al*., 2016; *Thompson et al*., 2016b]. Alternatively, the amorphous Si may have been a result of postdepositional additions of Si in alkaline pH lake conditions [*Hurowitz et al*., 2017].

3.2.5. Big Sky and Greenhorn (Siccar Point Group-Stimson Formation-Bridger Basin Outcrop-Sandstone)

The Big Sky and Greenhorn samples were acquired (sols 1120 and 1137, respectively) from the dominant crossbedded eolian sandstone facies of the Stimson formation in the Bridger Basin outcrop area (Figures 1, 2, and 9). The Stimson formation lies unconformably over the Murray formation (Figure 2) [*Fraeman et al*., 2016]. The BS and GH sampling site are ~250 m to the south of and ~8 m higher stratigraphically than Buckskin. The dark gray Big Sky sample was assumed to be representative of typical unaltered Stimson eolain sandstone with a total chemistry similar to average Mars crustal composition [*Yen et al*., 2017]. The Big Sky mineralogy is consistent with a basaltic origin, but in contrast to Rocknest eolian sediments, the Big Sky sample has substantially more magnetite and no olivine [*Yen et al*., 2017]. The Greenhorn sample extraction site is ~1.9 m to the southwest of Big Sky and occurs in a lighter gray to white band ~75 cm wide associated with a fracture that crosscuts the otherwise dark gray crossbedded sandstone represented by Big Sky (Figure 9). The Greenhorn sample is interpreted to be chemically altered compared to BS as indicated by its lower Mg, Al, Fe, Mn, Ni, and Zn suggesting that Greenhorn has been leached by fluids that passed through the fracture and adjacent pores [*Yen et al*., 2017]. The Greenhorn sample has higher Si and S than Big Sky, indicating that it underwent a complicated alteration history involving loss and gain of constituents. Greenhorn consists of less feldspar and pyroxene and more anhydrite and X-ray amorphous material than Big Sky [*Yen et al*., 2017].

4. Results/Discussion

4.1. H_2O

All samples evolved water (0.9 ± 0.3 to 2.5 ± 1.6 wt %) during SAM-EGA analysis (Figure 10 and Table S1). Water evolved less than ~200°C could be the release of adsorbed H_2O [e.g., *Tan et al*., 1986]. Water

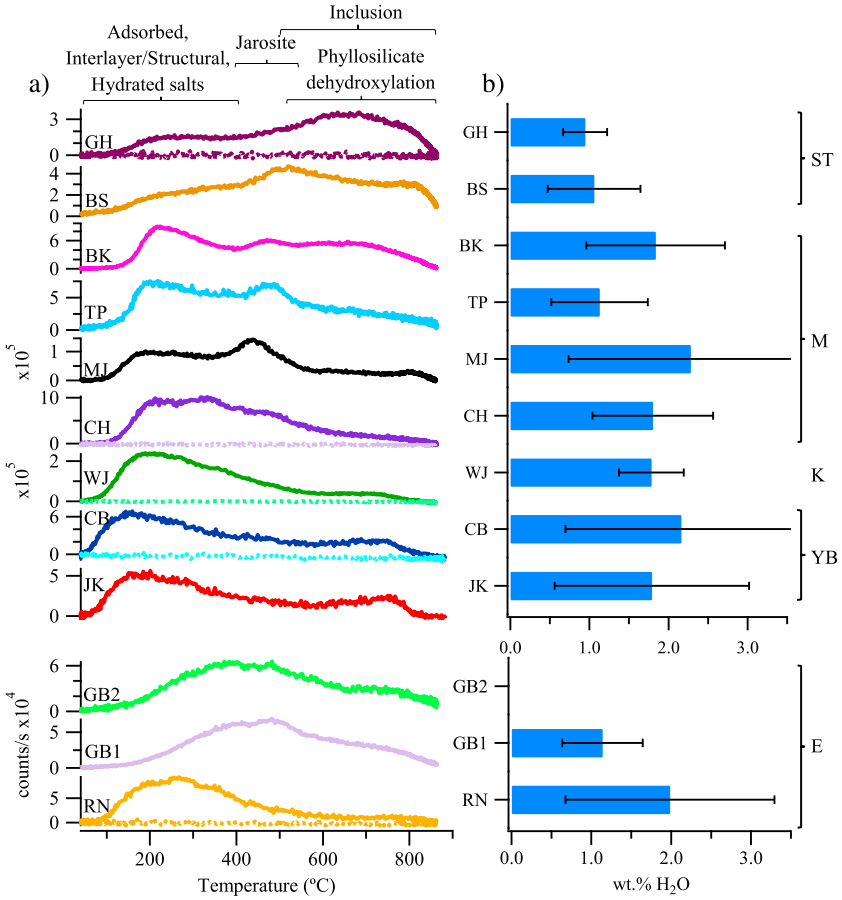

Figure 10. (a) Evolved water (m/z 20) (c/s) versus temperature as detected by the SAM-EGA. Dotted plots refer to empty cup runs that were run before sample analysis. *Y* axis scale is 10^4 c/s except where noted. Temperature ranges for source(s) of evolved water are noted with brackets. (b) Total evolved water content detected by the SAM-EGA. GB2 has no associated content as amount of soil delivery was not known. Far right bracketed notation refers to windblown eolian material (E) and sedimentary rock formations (Figure 2) Yellowknife Bay (YB), Kimberly (K), Murray (M), and Stimson (ST).

evolved between 100 and 300°C may have contributions from interlayer water [*Borchardt*, 1989] derived from smectite as in CB and JK [*Vaniman et al.*, 2014], and 2:1 phyllosilicates in WJ, CH, and MJ [*Treiman et al.*, 2016; *Rampe et al.*, 2016. Hydrated salts, such as bassanite in JK, CB, and WJ [*Vaniman et al.*, 2014; *Treiman et al.*, 2016] and oxychlorine salts, likely occur in all samples based on SAM observations (see below), and these could also contribute water released below 350°C. Dehydroxylation of small amounts of akaganeite detected by CheMin in JK, CB, and possibly WJ could also release some low-temperature H_2O [*Ming et al.*, 2014; *Vaniman et al.*, 2014; *Treiman et al.*, 2016]. Finally, X-ray amorphous phases, detected by CheMin in all samples [*Bish et al.*, 2013; *Vaniman et al.*, 2014; *Treiman et al.*, 2016; *Achilles et al.*, 2017; *Morris et al.*, 2016; *Rampe et al.*, 2017; *Yen et al.*, 2017], such as poorly crystalline aluminosilicate (e.g., allophane) or amorphous silicate (e.g., opal-A), and/or nanophase oxides/oxyhydroxides (e.g., ferrihydrite), could evolve H_2O in the <~450°C range.

Dehydroxylation may have yielded the evolved water above 450°C. The shoulders or peaks near 450–500°C in the CH, MJ, and TP traces can be attributed to dehydroxylation of H_2O from jarosite. The BK sample has a similar water feature at this temperature (Figure 10), but BK had no detectable jarosite in the CheMin data, suggesting either that jarosite is present but is below CheMin detection limits or the water is derived from some other source. Water evolved between 650 and 800°C from CB, JK, WJ, and MJ is interpreted to have been derived from the dehydroxylation of the phyllosilicates detected by CheMin [*Ming et al.*, 2014; *Vaniman et al.*, 2014; *Treiman et al.*, 2016; *Rampe et al.*, 2017].

The wide temperature water release >~500°C in BK, BS, and GH was attributed to inclusion water in the X-ray amorphous phases detected in these materials. The X-ray diffraction amorphous features in BK and GH suggest a more silica rich amorphous fraction than other samples, which exhibits X-ray diffraction features more consistent with a basaltic glass [*Bish et al*., 2013; *Vaniman et al*., 2014; *Treiman et al*., 2016; *Achilles et al*., 2017; *Morris et al*., 2016; *Rampe et al*., 2017; *Yen et al*., 2017]. Inclusion water in basaltic and rhyolitic (Si-rich) glass phases can evolve above 500°C [*Westrich*, 1987; *Pineau and Javoy*, 1994; *McAdam et al*., 2016].

4.2. H_2

Hydrogen (H_2) was evolved over a wide temperature range from all samples (Figure 11). Rocknest, JK, CB, BS, GH, GB1, and GB2 evolved H_2 mostly above 400°C. Windjana through BK evolved most of their H_2 between ~100°C and ~300 to 700°C. GB1 also had a low contribution of H_2 in this temperature range. This low- to middle-temperature H_2 in WJ to BK is likely related to water fragmentation in the mass spectrometer because these H_2 releases tend to follow evolution of water (Figure 10a). This low-temperature H_2 attributed to water fragmentation in the mass spectrometer was also present in JK and CB. This low-temperature H_2 is not apparent in JK and CB because it is a minor release compared to the higher-temperature JK and CB H_2 releases in Figure 11a and is difficult to resolve due to the large offset in the *y* axis compared to the WJ and BK curves.

Possible sources of these H_2 releases are serpentinization-type reactions, inclusion H_2 (MJ and BK only) and/or refractory organic carbon. Serpentinization-type reactions involving Fe(II)-containing phases (e.g., iron sulfides, olivine, and magnetite) and evolved water during SAM analysis could produce H_2 [e.g., *Sleep et al*., 2004; *McCollom and Bach*, 2009; *Mayhew et al*., 2013]. The subtle yet sharp H_2 releases at 590 and 650°C in MJ and BK, respectively (Figure 11a), could also be attributed to inclusion H_2 in a mineral phase. Refractory carbon phases could also contribute to H_2 evolution. Hydrogen gas evolution from refractory carbon phases has been documented to occur between 350 and 850°C [e.g., *Campbell et al*., 1980]. Refractory magmatic carbon phases have been detected in Martian meteorites [*Leshin et al*., 1996; *Grady et al*., 2004; *Steele et al*., 2012; *Agee et al*., 2013], suggesting that these carbon phases could contribute to the evolved H_2 in the Gale samples.

Evolved H_2 observed above 800°C in the RN and WJ to GB samples (Figure 11a) was attributed to an instrument effect. Examination of empty cup runs including the CB blank in oven 1 indicates a weak broad release of H_2 beginning at 300 to 700°C (Figure 11a). The greater *y* axis scale for the CB blank relative to the subsequent blanks does not permit the visualization of the broad H_2 release in the CB blank. This broad high-temperature release during the empty cup runs could, for reasons not yet known, be magnified in the presence of a sample. If this was the case, why this >800°C release was not observed in JK and CB is not clear, though this >800°C H_2 release was observed from RN (Figure 11a)? The SAM instrument contains two nickel alloy (Inconel 693) ovens and analyses on the SAM Testbed which uses nickel alloy ovens similar to the SAM flight ovens also exhibit these trends of high-temperature H_2 (data not shown). Analyses of the same samples in other non-Inconel containing ovens, however, often do not have these >800°C H_2 releases. This suggests an instrument effect that could be related to high-temperature Ni-alloy reactions with residual water (similar to serpentinization) to form H_2.

The source of the variations in H_2 abundances and H_2 evolution temperatures between samples is complex (Figure 11 and Table S2). These variations were likely related to water evolution temperature from the sample, the mineralogy of the Fe^{2+} phases that can promote serpentinization reactions in the oven, and type of carbon phase present. Other factors affecting H_2 evolution can be attributed to other evolved gases that may react with water and H_2 to inhibit or enhance the H_2 detection. Laboratory investigations using the appropriate analog materials and oven conditions are required to more fully understand the H_2 release phenomena at all temperatures.

4.3. SO_2

All samples evolved SO_2 mostly above 500°C with minor SO_2 evolution below 500°C in CB and GB2 (Figure 12a). Minor SO_2 evolutions below 500°C were consistent with oxidative sulfide decomposition directly to SO_2 [e.g., *Pelovski and Petkova*, 1999; *Ming et al*., 2014]. CheMin analyses showed ~1 wt % pyrrhotite (FeS) in CB, while sulfides in GB2 were not detected and were presumed to occur at concentrations below CheMin detection

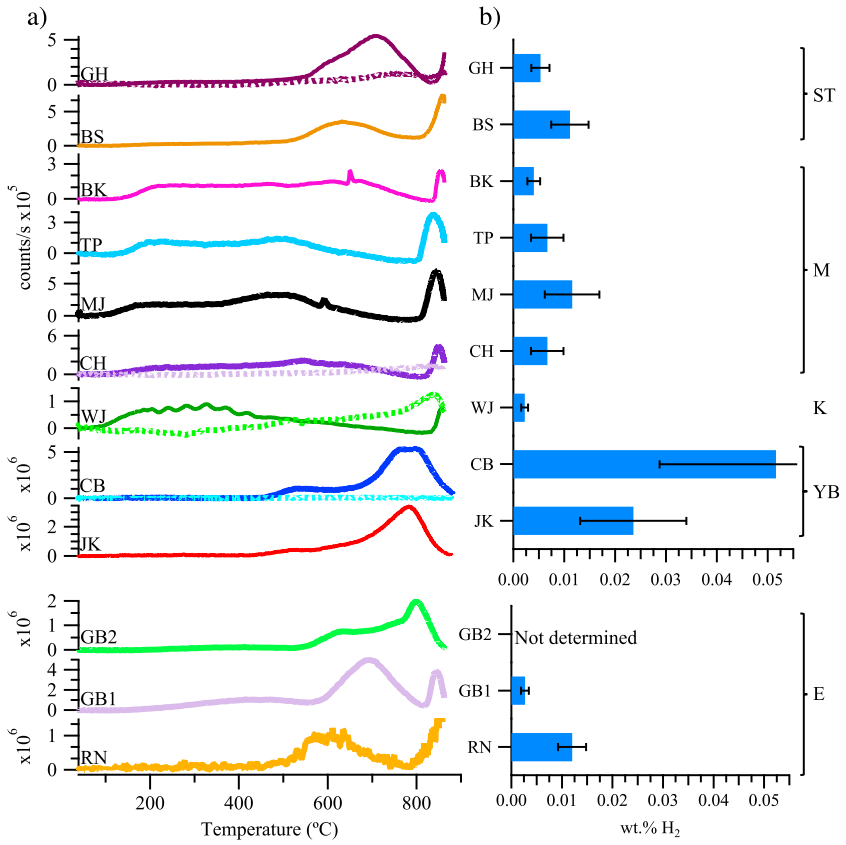

Figure 11. (a) Hydrogen (H_2, m/z 2) (c/s) versus temperature as detected by the SAM-EGA. *Y* axis scale is 10^5 c/s except where noted. Dotted plots refer to empty cup runs that were run before sample analysis. (b) Total evolved H_2 content. Far right bracketed notation refers to windblown eolian material (E) and sedimentary rock formations (Figure 2) Yellowknife Bay (YB), Kimberly (K), Murray (M), and Stimson (ST).

limits. The O_2 (Figure 17a) for sulfide oxidation was derived from oxychlorine decomposition that coincides with the <500°C SO_2 evolutions [*Ming et al.*, 2014].

The evolution of SO_2 above 500°C was consistent with the presence of Fe and/or Mg sulfate ranging from crystalline (e.g., jarosite) to amorphous sulfate as well as adsorbed sulfate forms [*McAdam et al.*, 2014]. The shapes of the major SO_2 release profiles above 500°C vary between samples, but several samples have two or more "peaks" within the broad temperature release (e.g., RN, CB, GH, and MJ), from ~500 to 700°C and >700°C (Figure 12a). The lower temperature peaks were consistent with Fe sulfate phases that typically decompose between 500 and 700°C [e.g., *McAdam et al.*, 2014]. Magnesium sulfate, if hydrated, will dehydrate below 500°C and then decompose at temperatures higher than those reached by SAM analyses [*Scheidema and Taskinen*, 2011]. However, when mixed with other phases, the thermal decomposition temperature of Mg sulfate is known to drop to within the SAM temperature range and likely dominates SO_2 releases above 700°C [*Mu and Perlmutter*, 1981a; *McAdam et al.*, 2016].

The presence of multiple peaks at select temperatures within the Fe sulfate or Mg sulfate temperature range (e.g., BS, BK, MJ, and GB2, Figure 12a) has the potential to be utilized to further identify specific Fe sulfate and Mg sulfate species [e.g., *McAdam et al.*, 2014]. The identification of specific Fe sulfate or Mg sulfate species from the evolved SO_2 detections will require extensive laboratory analog analyses that is beyond the scope of this work.

When crystalline sulfate species (e.g., jarosite detected by CheMin in CH, MJ, and TP) cannot account for all the evolved SO_2, then other sources of SO_2 are possible, including X-ray amorphous materials (e.g., amorphous sulfates), adsorbed sulfates, S phase inclusions in minerals or glass, oxidation of sulfide phases, or trace crystalline sulfur phases present below CheMin detection limits. X-ray amorphous materials (30–60 wt %)

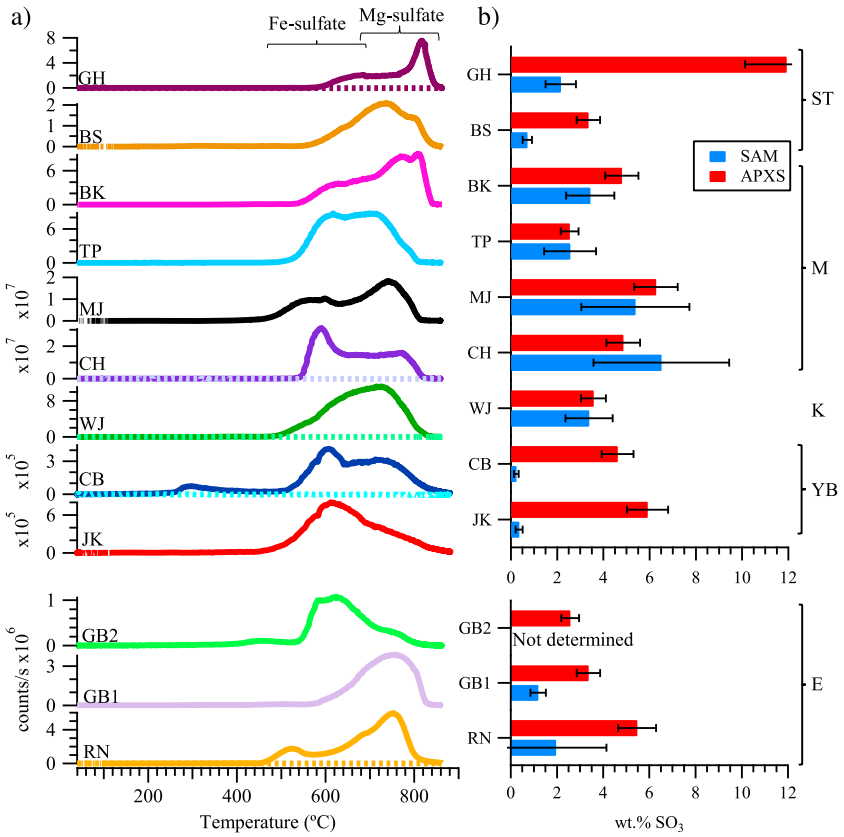

Figure 12. (a) Evolved SO_2 (m/z 64) (c/s) versus temperature as detected by the SAM-EGA. Dotted plots refer to empty cup runs that were run before sample analysis. Termperature ranges of SO_2 sources are indicated in brackets. *Y* axis scale 10^6 c/s except where noted. (b) Evolved SO_2 converted and reported as SO_3 (SAM) and compared to APXS measured SO_3 content. Far right bracketed notation refers to windblown eolian material (E) and sedimentary rock formations (Figure 2) Yellowknife Bay (YB), Kimberly (K), Murray (M), and Stimson (ST).

containing S (reported as 2–12 wt % SO_3) are present and could contribute significantly to SAM-EGA S detections [e.g., *Blake et al.*, 2013; *Vaniman et al.*, 2014; *Morris et al.*, 2016; *Treiman et al.*, 2016; *Rampe et al.*, 2017; *Yen et al.*, 2017]. Sulfate adsorbed onto iron (hydr) oxides is commonly observed in terrestrial environments [e.g., *Aylmore et al.*, 1967; *Parfitt and Smart*, 1978; *Rampe et al.*, 2016] and would not be detected by XRD if such sulfates were present in Gale Crater. The CheMin detection of pyrrhotite (FeS) in JK and CB indicate that the >500°C SO_2 could result from iron sulfate derived from sulfide oxidation by O_2 evolving from (per) chlorate at lower temperatures or oxidation of any sulfide remaining at higher temperatures as a result of incomplete oxidation below 500°C [*McAdam et al.*, 2014].

Other possible phases that could contribute to evolved SO_2 include Al sulfates or organo S-bearing phases [e.g., *Mu and Perlmutter*, 1981a; *McAdam et al.*, 2014]. CheMin and APXS data sets did not provide compelling mineralogical or geochemical evidence for the presence of Al sulfates though Al sulfates do form in acidic environments similar to Fe sulfates [*Lindsay*, 1979] and could be present at low concentrations. The oxidation of sulfur-bearing organics from O_2 derived oxychlorine phases could also contribute to SO_2 releases [*McAdam et al.*, 2014]. If all the evolved CO and CO_2 in WJ (~2373 μgC/g) was derived from indigenous carbon sources, up to 200 μg S/g could accompany this carbon and thus could contribute a small fraction to SAM-S (<0.05 wt % SO_3) (assumes 12.3 C/S wt % ratio from Murchison meteorite analyses) [*Okumura and Mimura*, 2011].

The presence of Ca sulfate in most samples (RN, JK, CB, BS, GH, and GB) [*Bish et al.*, 2013; *Vaniman et al.*, 2014; *Morris et al.*, 2016; *Yen et al.*, 2017] caused the amounts of S detected by SAM (SAM-S) to be less than the amounts of S detected by the APXS (APXS-S) (Figure 12b and Table S3). This is because all Ca sulfates decomposes at temperatures beyond the SAM range and thus cannot be detected by SAM [e.g., *Mu and Perlmutter*,

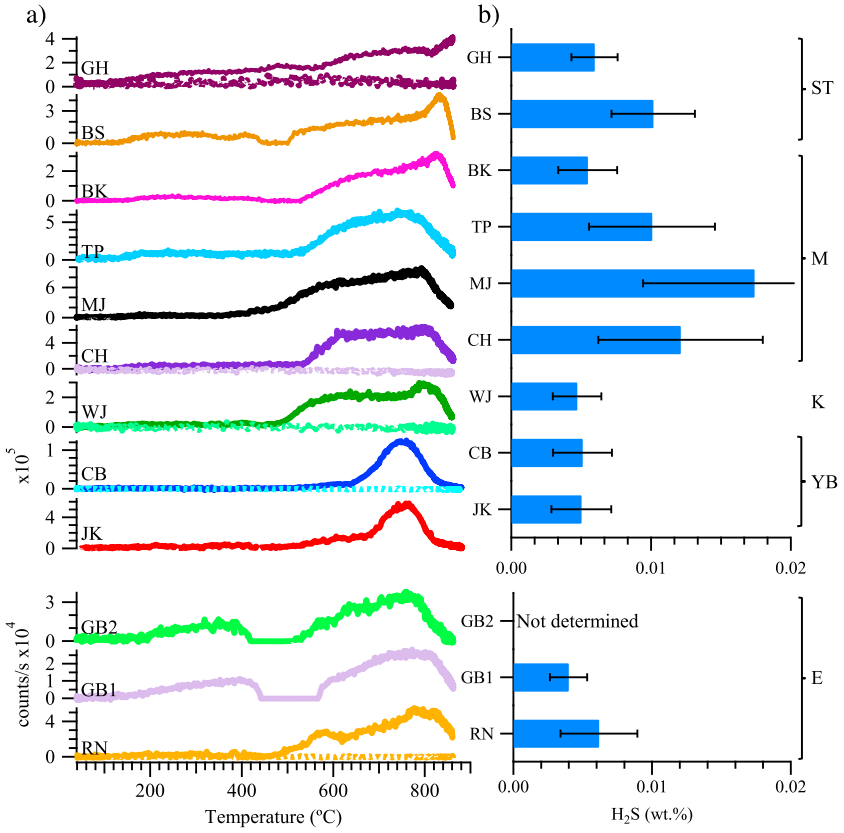

Figure 13. (a) Hydrogen sulfide (m/z 34) (c/s) versus temperature as detected by the SAM-EGA. Dotted plots refer to empty cup runs that were run before sample analysis. *Y* axis scale is x10^4 c/s except where noted. (b) Evolved hydrogen sulfide (H_2S) content. Far right bracketed notation refers to windblown eolian material (E) and sedimentary rock formations (Figure 2) Yellowknife Bay (YB), Kimberly (K), Murray (M), and Stimson (ST).

1981a; *McAdam et al.*, 2014]. When SAM-S and APXS-S contents were similar, Ca sulfate was either not detected by CheMin, or its detection was questionable (e.g., WJ, CH, MJ, and TP) [*Rampe et al.*, 2017; *Treiman et al.*, 2016]. For the WJ, CH, MJ, and TP samples, SAM-EGA is capturing all the APXS detected S (Figure 12b) which was determined to be mostly associated with Fe and/or Mg [*Treiman et al.*, 2016; *Rampe et al.*, 2017].

4.4. H_2S

The majority of H_2S was evolved at temperatures greater than 500°C (Figure 13a), though a gradual rise in H_2S evolution began at ~150°C in many samples (e.g., CH TP, BK, BS, GH, and GB). The GH sample, unlike the other samples, gradually released increasing H_2S throughout the entire SAM-EGA temperature range (Figure 13a).

The source of H_2S could be derived from H_2O and/or HCl reactions with sulfides in the sample (reactions (1) and (2)) [e.g., *Uno*, 1951; *Ingraham et al.*, 1972].

$$FeS + H_2O \rightarrow H_2S + FeO \quad (2)$$

$$FeS + 2HCl \rightarrow H_2S + FeCl_2. \quad (3)$$

Releases of H_2O and HCl occurred at similar temperatures as the H_2S releases especially at high temperature (Figures 10a and 18a), suggesting hydrogen from HCl or H_2O could be reacting with sulfide-bearing phases that may not have been completely oxidized or decomposed at lower temperatures. Pyrrhotite was detected in JK and CB and thus could react with water or HCl to evolve H_2S [*Ming et al.*, 2014]. Sulfide minerals were not detected in the other samples, but these sulfides could occur below CheMin detection limits or occur in the X-ray amorphous phase(s). Basaltic and silicic glasses can contain reduced sulfur [e.g., *Mathez*, 1976; *Paris*

et al., 2001] that might contribute to reactions that evolve H_2S. Other possible sulfides sources include nanophase sulfides or organic S-bearing phases that can occur in meteoritic materials [*Dai and Bradley*, 2001; *Sephton*, 2002; *Okumura and Mimura*, 2011] which are expected to be incorporated in Martian surface material [e.g., *Flynn*, 1996].

Evolved gas reactions between H_2 and SO_2 are another possible source of H_2S (reaction (3)) [*Arutyunov et al*., 1991; *Binns and Marshall*, 1991; *McAdam et al*., 2014].

$$SO_2 + H_2 \rightarrow H_2S + O_2. \quad (4)$$

The bulk of H_2S is released at similar temperatures, whereas most of the SO_2 and H_2 evolved together in several samples (e.g., JK, CB, BS, and GH) (Figures 11a and 12a) indicating that reaction (3) could also be occurring in those samples.

The "flat" gap between 400 and 550°C in BS, GB1, and GB2 was an artifact caused by the correction for the oxychlorine $^{18}O^{16}O$ isotopologue (Figure 13a). Contributions to m/z 34 from oxychlorine $^{18}O^{16}O$ isotopologue and sulfate ^{34}S isotopologue were subtracted from all m/z 34 plots as discussed in section 2.2. This feature was observed in these three samples because O_2 was observed at higher temperatures and at higher intensity than most other samples. Furthermore, m/z 34 attributed to H_2S achieved a higher intensity than most samples below and above the temperatures where the correction was applied. These factors all conspired to result in the effect of "cutting" into the H_2S evolution. Subtracting out less O_2 ($^{18}O^{16}O$) would result in peak in the gap that is clearly attributed to decomposition of oxychlorine.

The complexity of reactions between evolved gases and solid phases during SAM-EGA demonstrates that laboratory analysis of analog materials will be required to determine the most likely sources of H_2S in the Gale Crater samples. For example, the JK and CB samples have the only CheMin detections of a mineral iron sulfide (pyrrhotite), yet they have the some of the lowest H_2S content along with WJ (Figure 13b and Table S4). The other samples could have higher X-ray amorphous sulfide content that is undetectable by CheMin. The sulfides in CB could have undergone more oxidation due to greater O_2 evolution than the other samples (Figure 17b), thus obscuring the H_2S content that otherwise would have been evolved from CB.

4.5. NO (m/z 30).

SAM detected nitrates (0.002 ± 0.005 to 0.06 ± 0.03 wt %) in all sediments as indicated by evolved NO (Figure 14a). Multiple peak NO releases suggest that multiple cation species may be associated with nitrates in the Martian sediments. Fe-bearing nitrates tend to evolve NO at lower temperatures followed by Mg-, Ca-, Na-, and K-bearing nitrates at correspondingly higher temperatures [e.g., *Gordon and Campbell*, 1955; *Mu and Perlmutter*, 1982; *Ettarh and Galwey*, 1996; *Stern et al*., 2015]. However, the Fe-bearing phases like hematite, magnetite, and nanophase Fe oxides and oxychlorine phases present in the Gale materials have the potential to lower nitrate thermal decomposition temperatures relative to nitrates in the absence of such phases [*Hoshino et al*., 1981; *Navarro-González et al*., 2013]. Thermal shock processes involving impact events or lighting acting on atmospheric N_2 have been invoked to be the main sources of nitrates on Mars [e.g., *Mancinelli*, 1996; *Segura and Navarro-González*, 2005; *Manning et al*., 2008].

Despite the calculated instrument background contributions to NO in the Gale samples, SAM-EGA detected sufficient NO to indicate the presence of nitrate (Figure 14b and Table S5). The only cases where calculated background contributions could account for most of the evolved NO are in the CH and WJ samples. The CH had nearly as much background NO detected as JK but because CH had much less total NO detected, most of its detected NO could be attributed to background sources (Figure 14b). The WJ sample had much less total NO detected and despite its relatively lower background NO, corrected NO contributions resulted in the second lowest nitrate level.

4.6. CO_2

Carbon dioxide evolved over most of the SAM temperature range with candidate sources that include atmospherically adsorbed CO_2, organic carbon, carbonate, CO_2 inclusions in mineral or glass phases, and SAM background (Figure 15) [*Macpherson and Mattey*, 1994; *Grady et al*., 2004; *Cannon et al*., 2012; *Steele et al*., 2012; *Glavin et al*., 2013; *Leshin et al*., 2013; *Ming et al*., 2014; *Eigenbrode et al*., 2014; *Freissinet et al*., 2015]. The presence of adsorbed CO_2 onto Martian regolith has long been proposed [e.g., *Fanale and Cannon*,

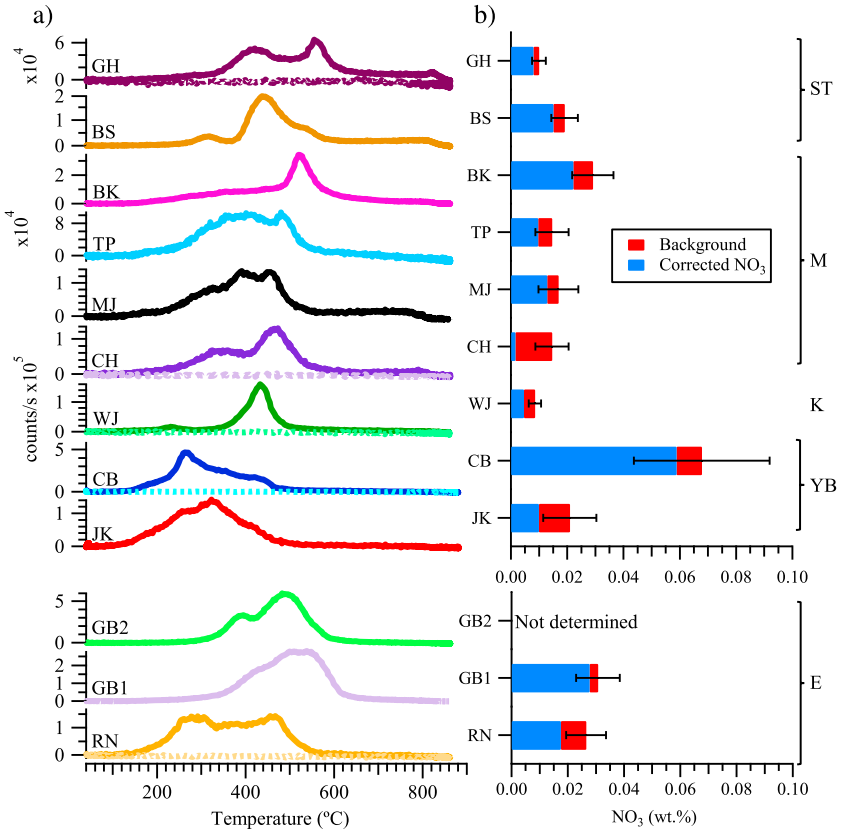

Figure 14. (a) Evolved NO (m/z 30) (c/s) versus temperature as detected by the SAM-EGA. Dotted plots refer to empty cup runs that were run before sample analysis. *Y* axis scale is 10^5 c/s except where noted. (b) Nitrate content (wt % NO_3^-) calcuated from evolved NO. Corrected contributions of nitrate from sample are in blue with estimated contribution from background in red. Far right bracketed notation refers to windblown eolian material (E) and sedimentary rock formations (Figure 2) Yellowknife Bay (YB), Kimberly (K), Murray (M), and Stimson (ST).

1974; *Zent and Quinn*, 1995], and it is likely that any adsorbed CO_2 present on Gale sediments could contribute to CO_2 evolved below 250°C [*Hochstrasser and Antonini*, 1972; *Jänchen et al.*, 2009].

The possible types of organic C that could contribute to Gale Crater CO_2 include simple organic carbon (<350°C), refractory macromolecular carbon (300–600°C), trapped organics (>600°C), and magmatic carbon (>600°C) [e.g., *Campbell et al.*, 1980; *Espitalié et al.*, 1984; *Grady et al.*, 2002, 2004; *Steele et al.*, 2012; *Francois et al.*, 2016]. Combustion of organics can explain some of the CO_2 releases. Crosshatched bars underneath each CO_2 release in Figure 15a correspond to temperatures of O_2 releases, while tick marks indicate position of O_2 peaks derived from the thermal decomposition of oxychlorine phases. This suggests that O_2 releases coinciding with CO_2 releases is consistent with combustion as a contributor to CO_2. The CB samples evolved chlorohydrocarbons that were detected by GCMS in the 150 to 350°C temperature range [*Freissinet et al.*, 2015] indicating organic combustion likely contributed to CO_2 in CB. The JK sample could represent an extreme case where all the O_2 was consumed by combustion resulting in a dip of the O_2 release (dotted tick mark) between the two O_2 peaks (solid tick marks) [*Ming et al.*, 2014] (Figures 15a and 17a). The O_2 dip (dotted vertical marker in Figure 15a) coincides with the main CO_2 release in JK.

Decarboxylation of organic compounds is another potential source of CO_2 over a broad temperature range (150 to 800°C) [*Mu and Perlmutter*, 1981b; *Dollimore*, 1987; *Okumura and Mimura*, 2011; *Eigenbrode et al.*, 2014]. Oxygen-bearing carbonyl and carboxyl groups in refractory organic material have been detected in Tissint Martian meteorite [*Steele et al.*, 2014]. Furthermore, oxygen-bearing organics are commonly found in carbonaceous chondrites [*Okumura and Mimura*, 2011], which through meteoritic infall, are expected to occur on the Martian surface [*Flynn*, 1996]. Alternatively, organics of either Martian or exogenous sources could have been oxidized to carboxylic acids [e.g., mellitic acid (RCOOH), acetate ($CH_3CO_2^-$), and oxalates

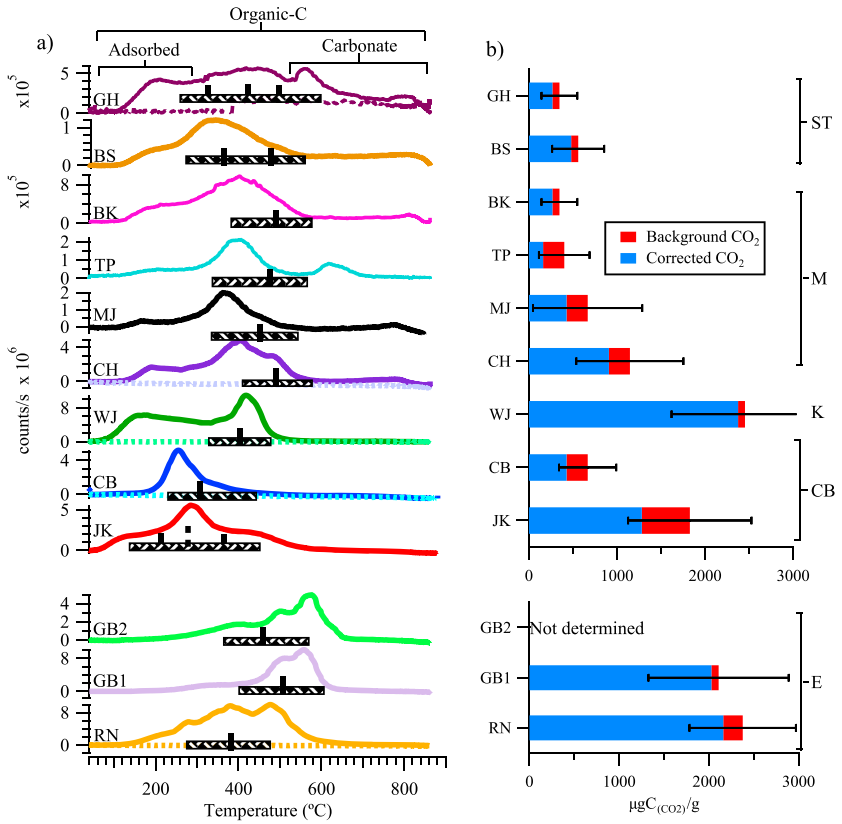

Figure 15. (a) Evolved CO_2 (m/z 44) (c/s) versus temperature as detected by SAM-EGA. Temperature ranges of possble CO_2 sources are indicated in brackets. Cross-hatched bars indicate temperature range of O_2 evolution. Solid tick marks on bars indicate O_2 peak temperatures from Figure 17a. The dashed tick mark in JK indicates the O_2 release dip temperature that corresponds with JK CO_2 peak temperature. *Y* axis scale is 10^6 c/s except where noted. (b) Carbon content ($\mu gC_{(CO2)}/g$) derived from evolved CO_2. CO_2 contribution from sample in blue with estimated contribution from background in orange. Far right bracketed notation refers to windblown eolian material (E) and sedimentary rock formations (Figure 2) Yellowknife Bay (YB), Kimberly (K), Murray (M), and Stimson (ST).

($C_2O_4^{2-}$)] by oxidative radiolytic weathering, or other oxidation processes on the Martian surface [*Benner et al.*, 2000; *Eigenbrode et al.*, 2014; *Applin et al.*, 2015].

Carbon dioxide releases above 600°C were consistent with decomposition of organics trapped in minerals [e.g., *Aubrey et al.*, 2006; *Bowden and Parnell*, 2007]. Coprecipitated phthalic acid with Mg sulfate was demonstrated to be protected from combustion by oxychlorine derived O_2 below 600°C [*Francois et al.*, 2016]. Carbon dioxide evolution only occurred when Mg sulfate decomposed at ~700°C, and the phthalic acid subsequently combusted. CO_2 releases associated with natural jarosite thermal decomposition have also been demonstrated [*Lewis et al.*, 2015]. The presence of Fe and/or Mg sulfate in most samples suggests that any organics trapped within Martian sulfate minerals, if present, could have contributed to evolved CO_2 at these high temperatures.

Combustion of magmatic carbon (MC) was another potential source of low-level CO_2 above 600°C [*Pineau and Javoy*, 1994; *Grady et al.*, 2004; *Steele et al.*, 2012] in CH, MJ, BK, BS, and GH. Magmatic carbon refers to carbon that occurs in inclusions or vesicles of mineral or glass phases and along grain surfaces [*Grady et al.*, 2004]. Magmatic carbon can occur as graphite, carbynes, polycyclic aromatic hydrocarbons, and/or "amorphous" carbon [*Mathez and Delaney*, 1981]. Magmatic carbon has been detected in several Martian meteorites through pyrolysis and combustion analyses above 600°C and by Raman imaging [*Leshin et al.*, 1996; *Grady et al.*, 2004; *Steele et al.*, 2007, 2012, 2016; *Agee et al.*, 2013]. The CH, MJ, and BK samples had additional O_2 releases at these temperatures due to sulfate decomposition (see section 4.8 below) indicating that

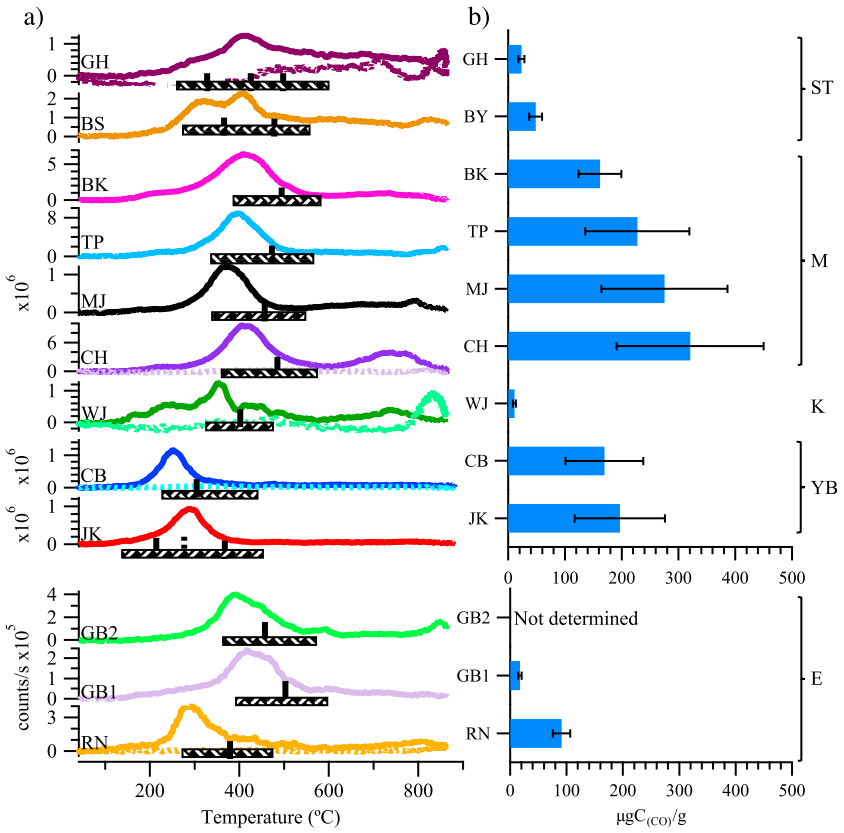

Figure 16. (a) Evolved CO (m/z 28) (c/s) versus temperature as detected by the SAM-EGA. Dotted plots refer to empty cup runs that were run before sample analysis. Cross-hatched bars indicate temperature range of O_2 evolution. Solid tick marks on bars indicate O_2 peak temperatures from Figure 17a. The dashed tick mark in JK indicates dip in O_2 release that corresponds with JK CO_2 peak. *Y* axis scale is 10^5 c/s except where noted. (b) Carbon content (μg $C_{(CO)}$/g) derived from evolved CO. Far right bracketed notation refers to windblown eolian material (E) and sedimentary rock formations (Figure 2) Yellowknife Bay (YB), Kimberly (K), Murray (M), and Stimson (ST).

combustion of magmatic carbon caused by O_2 releases from sulfate decomposition in all samples could be possible. The nondetection of sulfate-derived O_2 in other samples does not necessarily mean that O_2 was not released. The possibility exists that undetected O_2 was released but was consumed by other processes such as oxidation of Fe^{2+} mineral phases (e.g., magnetite and pyroxenes) and/or organic combustion.

High-temperature (>600°C) evolved CO_2 in CH, MJ, BK, BS, and GH (Figure 15a) could also have contributions from CO_2 inclusions within mineral/glass phases [e.g., *Macpherson et al.*, 1999; *Manning et al.*, 2013]. The presence of 15–60 wt % amorphous material in the Gale Crater sediments of [e.g., *Bish et al.*, 2013; *Vaniman et al.*, 2014; *Morris et al.*, 2016] suggests that some of the high-temperature CO_2 could be derived from this amorphous material.

Carbonates are potential sources of CO_2 evolved from 450 to 800°C [*Leshin et al.*, 1996; *Sutter et al.*, 2012; *Cannon et al.*, 2012; *Leshin et al.*, 2013; *Ming et al.*, 2014]. The temperatures of the highest Gale CO_2 release peaks are consistent with Fe-rich carbonate for RN and CH, Mg-rich carbonate for TP, and Fe-Mg carbonate for GH and GB. The amounts of carbonates if present are low (<0.7 wt %) and below CheMin detection limits.

Reactions of evolved HCl with carbonates present in the sample could also have contributed to evolved CO_2 below 450°C [*Cannon et al.*, 2012]. Laboratory analysis of evolved HCl from thermally decomposing Mg-perchlorate has been shown to react with carbonates to evolve CO_2 below temperatures expected for thermal decomposition of carbonate. Evolved HCl observed between 200 and 500°C in CB, CH, TP, and BS (Figure 18) could have reacted with carbonate to contribute observed CO_2 in these samples. The coinciding evolution of CO with CO_2 (Figures 15 and 16) in these samples, however, suggests that organic C sources supports organic C sources of CO_2 in this temperature range as well. Nevertheless, evolved HCl reactions

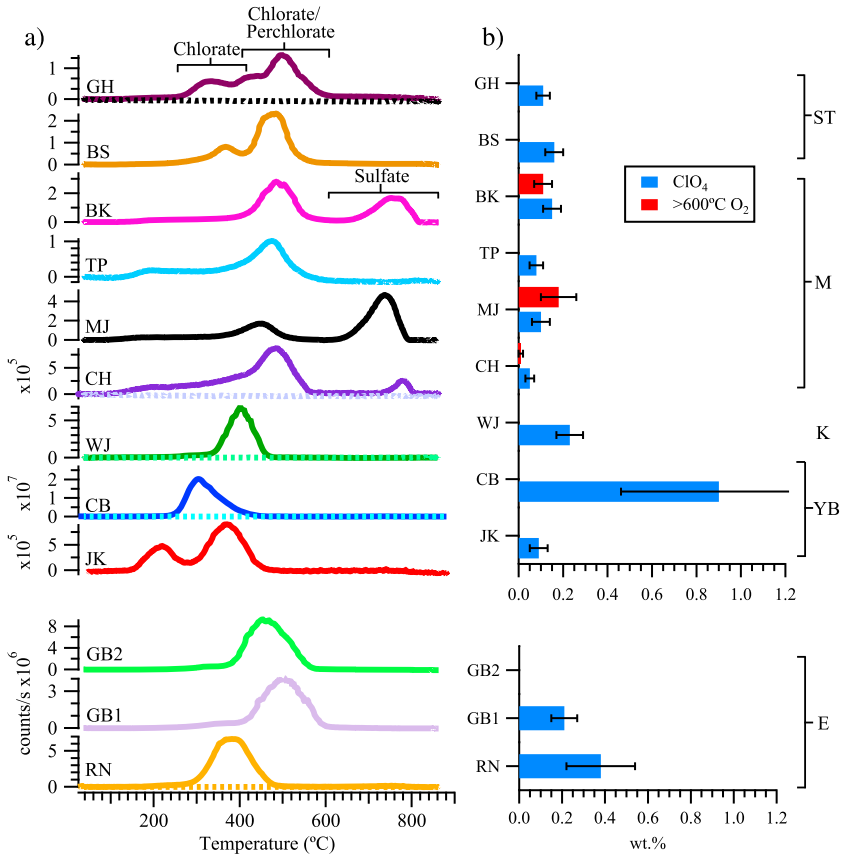

Figure 17. (a) Evolved O_2 (m/z 32) (c/s) versus temperature as detected by SAM-EGA. Dotted plots refer to empty cup runs that were run before sample analysis. Possible sources of O_2 are indicated in brackets. *Y* axis scale is 10^6 c/s except where noted. (b) Evolved O_2 content below 600°C calculated as perchlorate (ClO_4) and calculated as O_2 above 600°C (>600C–O_2). Far right bracketed notation refers to windblown eolian material (E) and sedimentary rock formations (Figure 2) Yellowknife Bay (YB), Kimberly (K), Murray (M), and Stimson (ST).

with Gale Crater carbonates should be considered as potential contributors to evolved CO_2 at temperatures below 450°C.

Contributions of background CO_2 from the derivatization reagent MTBSTFA are also likely contributors to the evolved CO_2 at temperatures <600°C. When compared to the total evolved CO_2, the amount of background CO_2 indicated in orange in Figure 15b could not account for all of the evolved CO_2. Total CO_2 evolved from all samples except TP indicated that background CO_2 in the worst case would consist of less than 36% of the evolved CO_2 (Figure 15b). The TP sample evolved so little CO_2 that background CO_2 had the potential to contribute at least 60% evolved CO_2 to the TP release (Figure 15b). The 900 nmol background CO_2 estimate was applied to all samples regardless if they were single or triple portions [*Glavin et al.*, 2013]. Thus, the WJ, BK, BS, and GH have lower contributions to background relative to the other samples because these triple portion samples when normalized for comparison to single portions had less background CO_2 than the other single portion samples.

Most CO_2 (except in GB) was evolved below 450°C, which was consistent with CO_2 derived from organics. Excluding the possible background sources, the organic sources could be indigenous to Mars from igneous, hydrothermal, atmospheric or biological sources, or exogenous from interplanetary dust particles, cometary, or meteoritic infall [e.g., *Flynn*, 1996; *Jull et al.*, 2000; *Yen et al.*, 2006; *Heinrich et al.*, 2007; *Steele et al.*, 2007; *Leshin et al.*, 2013; *Ming et al.*, 2014; *Freissinet et al.*, 2015]. Carbonates (RN, TP, and GH) and MMC (CH, MJ, BS, and GH) are possible higher-temperature sources of CO_2. The GB sample is different than all other samples in that most CO_2 was evolved above 450°C suggesting GB CO_2 was derived from carbonate, although organics cannot be excluded.

The CO_2 carbon contents (160 ± 248–2373 ± 820 $\mu gC_{(CO2)}$/g; corrected for background CO_2) vary over a wide range (Figure 11b and Table S6). The highest CO_2 carbon contents occurred in the eolian RN and GB sediments and the JK mudstone and WJ sandstone, whereas the lowest contents were found in the TP, BK, and GH samples (Figure 15b). There appears to be a general trend of decreasing CO_2 carbon content with increasing elevation beginning with WJ (Figure 15b).

4.7. CO

Carbon monoxide was evolved from all samples over a wide temperature range (Figure 16). The majority of the CO evolved between 150 and 575°C and was mostly coincident with at least one of the CO_2 release peaks. The CO carbon content associated with CO_2 was always less than CO_2 (Figures 15b and 16b and Tables S6 and S7). Lower CO release intensities were evolved between 575 and 750°C in all samples except CB and JK where no major CO releases were observed at those temperatures.

The evolution of the CO was consistent with the presence of incomplete combustion of organics and/or oxygen-bearing organics in the Gale Crater materials. The oxygen-bearing organics as discussed for CO_2 can be derived from initially deposited oxygen-bearing organics [e.g., *Okumura and Mimura*, 2011; *Steele et al*., 2014] or organics (e.g., hydrocarbons) that oxidized to carboxylic acids from exposure to oxidizing conditions on the Martian surface [*Benner et al*., 2000]. Laboratory analysis of oxygen-bearing organics from thermal decomposition of carbonaceous chondrite and carboxylic acids demonstrates that the main CO and CO_2 releases can occur at the temperature ranges observed by SAM [e.g., *Dollimore*, 1987; *Okumura and Mimura*, 2011; *Eigenbrode et al*., 2014].

Evidence of background CO evolution was present in the blanks above 400°C and especially above 820°C (Figure 16a). Background CO releases above 400°C was observed in the GH blank and could be considered significant for GH and possibly WJ because these samples released so little overall CO. Comparison of the WJ and GH blank intensities to other sample intensities illustrates that background CO was not as significant contributor to overall CO releases. The consistency of background CO peaks above 820°C in the blanks suggests that CO peaks with similar intensities (e.g., GB, TP, and BS) (Figure 16a) could have significant contributions from background above 820°C. The source of background CO below 600°C could have contributions from MTBSTFA. The CO background sources above 600°C are unknown, and laboratory analog work will be required to understand this source.

The CO carbon content (11 ± 3 to 320 ± 130 μg $C_{(CO)}$/g) was variable throughout Gale Crater (Figure 16b and Table S7). The CO carbon content unlike CO_2 was low in RN and GB compared to the much higher CO carbon content in CH. Similar to CO_2, the CO carbon content decreased with elevation beginning with CH (Figure 16b).

4.8. O_2

Oxygen was evolved from all samples suggested the presence of oxychlorine phases like chlorate or perchlorate (0.05 ± 0.025 to 1.05 ± 0.44 wt % as ClO_4) (Figure 17 and Table S8). However, the O_2 peak temperatures were lower than what is typical of pure reagent grade Ca, Mg, Na, and K perchlorate and higher than what is expected for iron perchlorate [*Glavin et al*., 2013]. Alternatively, pure Mg, Ca, or Na chlorate have O_2 release temperatures that occur coincident with the O_2 releases from most of the Gale samples with the exception of the CB and low-temperature JK peaks [*Sutter et al*., 2014; *Clark et al*., 2016]. Iron phases detected in Gale Crater sediments could catalyze the perchlorate and/or chlorate thermal decomposition to lower temperatures; analyses of these mixtures have resulted in O_2 release temperatures consistent with those detected by SAM [*Rudloff and Freeman*, 1970; *Sutter et al*., 2015; *Clark et al*., 2016].

Thermal decomposition of sulfate was the likely source of the second high-temperature O_2 evolution in CH, MJ, and BK (Figure 17a). Unlike the other Gale sediments, the CH, MJ, and BK samples have two distinctive O_2 releases. The lower temperature (<600°C) O_2 releases in CH, MJ, and BK are attributed to an oxychlorine phase(s). The higher-temperature (>600°C) O_2 releases in CH, MJ, and BK were not attributed to an oxychlorine phase as this O_2 release temperature was typically too high for perchlorate and chlorate thermal decomposition. Although the high-temperature O_2 release profile does not correspond precisely with the SO_2 release profile, the high-temperature O_2 peak does correspond with at least one of the SO_2 peaks (Figures 12a and 17a). This suggests that sulfate decomposition described above could have supplied the

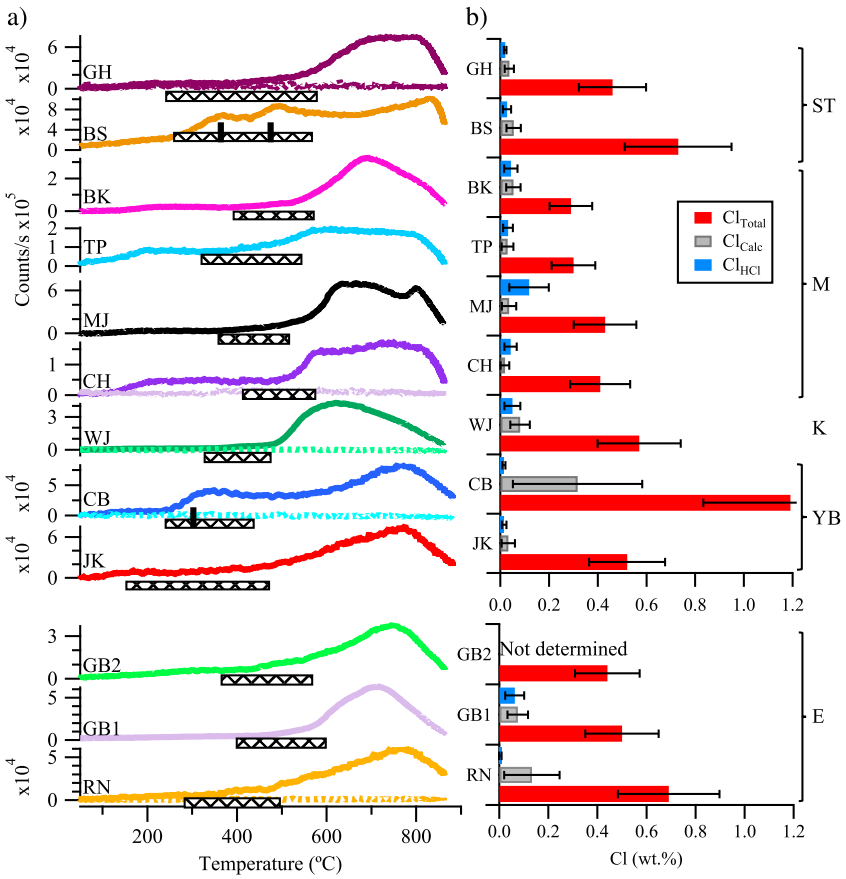

Figure 18. (a) Evolved HCl (m/z 36) (c/s) versus temperature as detected by SAM-EGA. Dotted plots refer to empty cup runs that were run before sample analysis. Hash marked bars indicate temperature range of O_2 evolution from Figure 17b. Solid tick marks on CB and BS bars indicate O_2 peak temperatures from Figure 17a. *Y* axis scale is 10^5 c/s except where noted. (b) Chlorine content from evolved HCl detected by the SAM-EGA (Cl_{HCl}), chlorine calculated from evolved O_2 as perchorate (ClO_4^-) (Cl_{Calc}), and total Cl detected by APXS (Cl_{Total}). Far right bracketed notation refers to windblown eolian material (E) and sedimentary rock formations (Figure 2) Yellowknife Bay (YB), Kimberly (K), Murray (M), and Stimson (ST).

high-temperature O_2. Magnesium sulfate and Fe sulfate (e.g., jarosite), which have been detected in the Pahrump rocks, commonly evolve O_2 upon thermal decomposition [e.g., *Gallagher et al.*, 1970; *Scheidema and Taskinen*, 2011; *Lewis et al.*, 2015].

$$\text{Dehydrated jarosite} \quad 2K_3Fe(SO_4)_3 \rightarrow 3K_2SO_4 + Fe_2O_3 + 3SO_2 + 1.5O_2. \tag{5}$$

Why the high-temperature O_2 release profile in CH, MJ, and BK does not follow the SO_2 release profile with same number of peaks or why high-temperature O_2 releases were not observed in the other samples was not clear. Complex reactions during SAM-EGA analysis between sulfate evolved O_2 and other mineral phases or evolved gases present in some Gale materials and not in others could inhibit O_2 detection. More work involving SAM-EGA analog analyses will be required to understand this inconsistency of high-temperature O_2 evolution.

The presence of multiple O_2 peaks between 250 and 500°C in BS and GH suggests that these sediments could possess chlorates and perchlorates or multiple cation phases of perchlorate and/or chlorate (Figure 17a). The cation present in the oxychlorine phase affects the decomposition temperature where perchlorate and chlorate decomposition temperatures tend to follow the order Fe perchlorate < Mg chlorate < Ca chlorate < Mg perchlorate < Ca perchlorate ~ Na chlorate < Na perchlorate < K chlorate < K perchlorate [e.g., *Glavin et al.*, 2013; *Sutter et al.*, 2015]. For example, one possible scenario for the three O_2 peaks in GH sediment was that GH possesses Mg chlorate, Mg perchlorate, and Ca perchlorate, all of which could yield three distinctive O_2 peaks in GH.

The content distribution of oxychlorine phases could be affected by one or more factors. The oxychlorine contents (as ClO_4^-) mostly range from 0.05 to 0.38 wt % with the CB material having the significantly highest content (1.05 wt % ClO_4^-, Figure 17b and Table S8). The source of all the sediments could simply have variation in oxychlorine content that causes the observed distribution. Postdepositional solutions enriched or depleted in soluble salts could raise or lower the soluble salt contents, respectively, of the Gale materials. Other post depositional oxidizing or reducing processes could also affect the oxychlorine contents [e.g., *Catling et al*., 2010; *Quinn et al*., 2013; *Wilson et al*., 2016]. More detailed analysis of the mineralogy and geochemistry coupled with laboratory analysis will be required to understand the nature and origins of the oxychlorine distribution in Gale Crater.

4.9. Hydrochloric Acid (HCl)

Hydrochloric acid was evolved from all Gale materials (0.004 ± 0.005 to 0.1 ± 0.08 wt % Cl_{HCl}) (Figure 18 and Table S9). All HCl evolved at temperatures greater than the initially evolved O_2 with the exception of the CB and BS samples. Hatched rectangles in Figure 18a indicate the temperature range of O_2 releases. The CB and BS samples evolved HCl with O_2 but also possessed a high-temperature (>600°C) HCl peak that was not associated with any O_2 release (Figures 17a and 18a).

The evolution of HCl with O_2 in the CB and BS samples suggests the presence of Mg perchlorate and/or Mg chlorate phases. Only the Fe and Mg oxychlorine species chlorate and perchlorate are known to release HCl. All other oxychlorine phases typically form corresponding chloride phases (e.g., $CaCl_2$, NaCl, and KCl) with no significant HCl evolution [e.g., *Marvin and Woolaver*, 1945; *Markowitz*, 1963; *Migdal-Mikuli and Hetmańczyk*, 2008; *Cannon et al*., 2012]. The temperature of O_2 and HCl evolution was likely too high to be Fe perchlorate or Fe chlorate [e.g., *Glavin et al*., 2013]. This suggests that Mg perchlorate or Mg chlorate are the best candidates for CB and BS.

The evolution of high-temperature HCl not associated with oxychlorine decomposition (Figure 18a) was consistent with water vapor reacting with vapor from melting chloride salts [e.g., *Fraisslera et al*., 2009].

$$CaCl_2(g) + H_2O(g) \rightarrow 2HCl + CaO. \quad (6)$$

The source of the chloride salts in the Gale materials was consistent with thermal decomposition products associated with Ca, Na, and/or K oxychlorine phases that decompose to chlorides [*Marvin and Woolaver*, 1945; *Markowitz*, 1963]. Chloride salts already in the Gale sediments may also be a source of Cl for reaction (5). The wide temperature range in which HCl was evolved was suggestive of water vapor reacting with a chloride that melted over a wide temperature range which could be attributed to impurities in the chlorides. Such impurities would be expected to reduce and broaden the chloride melting temperature [e.g., *Pavia et al*., 1982].

The Cl content derived from evolved HCl (Cl_{HCl}) did not always agree with the Cl content calculated from the amount of measured SAM-O_2 (Cl_{Calc}) assuming that all O_2 was derived from perchlorate (Figure 18b). The RN, JK, and CB samples had lower Cl_{HCl} than Cl_{Calc}, whereas the WJ CH, MJ, TP, BK, BS, GH, and GB materials had, within error, similar amounts of Cl_{HCl} and Cl_{Calc}. This suggests that the chloride salts produced from oxychlorine decomposition in the RN, JK, and CB samples did not completely react with water to yield HCl. The cause for this discrepancy is not known, and analog laboratory work will be required to understand this behavior.

The Cl_{Calc} was always lower than total Cl (Cl_{Total}) measured by APXS (Figure 18b and Table S9), indicating that there was a Cl component that does not occur as oxychlorine phases. Chlorine in Martian meteorites has been found to be associated with apatite, amphiboles, NaCl, biotite, scapolite, and glass [*Williams et al*., 2016, and references therein]. Apatite which was detected by CheMin in WJ, CH, MJ, and TP (0.8–2 wt %) cannot make up for the missing Cl because apatite provides only a fraction (<17%) of total Cl in those samples (assumes apatite Cl content detected in Mars meteorites, e.g., $Ca_5(PO_4)_3(Cl_{0.5}, F_{0.3}, OH_{0.2})$ [*Filiberto and Treiman*, 2009]). Amphiboles or scapolite are another a source of Cl in Martian meteorites [e.g., *Filiberto and Treiman*, 2009; *Filiberto et al*., 2014], yet no amphiboles or scapolite have been detected by CheMin. Phyllosilicates have been detected in Gale sedimentary rock [*Vaniman et al*., 2014; *Treiman et al*., 2016; *Rampe et al*., 2017]; however, no evidence of biotite has been detected. This leaves the remaining Cl component to reside in some glassy/amorphous component and/or in a crystalline phase that was below the

CheMin detection limits. If the remaining Cl component was crystalline NaCl or $CaCl_2$, it would amount to $<$1 wt % NaCl or $CaCl_2$, which was below CheMin detection limits.

5. Implications

5.1. Introduction

The SAM-EGA detections provide a substantial advancement in understanding the geochemical and mineralogical composition of the sediments and sedimentary rocks sampled in Gale Crater. The SAM-EGA analyses have corroborated detections of phyllosilicates and jarosite by CheMin and amorphous sulfate by CheMin/APXS and provided insight into the phases that bear water as detected by the DAN instrument [*Mitrofanov et al*., 2014]. SAM-EGA analyses have also been critical in detecting phases such as nitrate, oxychlorine, and organic/inorganic carbon that were not detected by other MSL instrumentation. The following section evaluates RN and GB eolian sediments, Sheepbed mudstone, Windjana sandstone, Murray mudstone, and the Stimson sandstone materials with a focus on highlighting notable evolved gas detections specific to SAM-EGA that assist in adding further understanding to the compositions and origins of Gale Crater sediments and sedimentary rock.

5.2. Rocknest/Gobabeb Eolian Sediments

Notable characteristics of RN and GB include relatively high CO_2 and NO releases and evidence of organic carbon and carbonate. There was also evidence for a grain size dependence of water type, SO_2 evolution temperatures, and possible carbon speciation.

The eolian RN and GB samples evolved CO_2 at temperatures consistent with the presence of organic C ($<$450°C) and carbonate (450–650°C) (Figure 15a). The GB sample is dominated by coarser grains ($>$100 μm) [*Ehlmann et al*., 2017] and released most CO_2 in the 450–650°C CO_2 range consistent with the presence of carbonate (~0.70 ± 0.1 wt % CO_3) though organic C cannot be completely excluded. Lower temperature ($<$450°C) CO_2 indicated that some organic C could be present in GB. The RN sample had significant fine-grained component (~40–60% $<$ 100 um) [*Minitti et al*., 2013] which evolved most CO_2 at temperatures consistent with organic C, whereas ~30% of its CO_2 is consistent with carbonate (~0.32 ± 0.05 wt % CO_3) [*Leshin et al*., 2013]. These results demonstrate a possible grain size dependence of carbon species in eolian sediment, where organic C and carbonate may mostly reside in fine-grained (~$<$100 μm) and coarser-grained (~$>$100 μm) eolian sediments, respectively.

The RN and GB eolian surface materials have some of the highest nitrate and CO_2 carbon contents measured to date (Figures 14b and 15b and Tables S5 and S6), which could indicate that other sources with high nitrate and carbon contents exist in Gale Crater. The coarser grained components (e.g., $>$100 μm) of RN and GB suggests that carbon and nitrate were mostly acquired from the erosion of local and regional sources. The amount of eolian dust ($<$10 μm) [*Morris et al*., 2006, and references therein] in RN is not known but a fine-grained component ($<$100 μm) (~40–60%; [*Minitti et al*., 2013]) is present indicating that RN could consist of some globally mixed nitrate- and carbon-bearing dust with similarly high C and N.

The overall water release profile for RN and GB differed, which is attributed to grain size distribution differences between the two samples. Rocknest released a greater amount of water below 200°C than GB (Figure 10a). The GB sediment material is dominated by $>$100 μm grain sizes [*Ehlmann et al*., 2017], whereas RN has a substantial $<$100 μm size fraction [*Minitti et al*., 2013]. The greater amount of fine-grained material in RN likely has a greater surface area that can retain more adsorbed water than the coarser grained GB material.

Grain size effects appeared to have an effect on SO_2 releases between the GB1 ($<$150 μm) and the GB2 (150 μm–1 mm) samples. The GB1 SO_2 release temperatures were consistent with SO_2 being derived from Mg sulfates, while the SO_2 release temperatures in the larger-grained GB2 were more consistent with releases from Fe sulfate phases (Figure 12a). The Murray material near to the GB samples contained Mg sulfate concretions that were also detected at Pahrump which may erode to $<$150 μm particle sizes and make contributions to the GB materials. CheMin detections of jarosite in the Pahrump material of the Murray formation may be the source of Fe sulfates indicated by the SAM-EGA for the larger particle GB2 sample.

5.3. Sheepbed Member-Yellowknife Bay Formation

The JK and CB mudstones had the highest evolved H_2 content which is consistent with the hypothesis that these lacustrine sediments were deposited under reducing conditions [*Grotzinger et al*., 2014; *Ming et al*., 2014]. The SAM-GCMS detection of organics and sulfur containing organics in CB [*Freissinet et al*., 2015] and the CheMin detection of Fe sulfide (pyrrhotite) only in JK and CB [*Vaniman et al*., 2014] highlight the reduced nature of the Sheepbed rocks. Hydrogen could be evolved from the thermal decomposition of hydrocarbons [*Campbell et al*., 1980] or through reactions of evolved water and Fe sulfides:

$$4FeS + 2H_2O \rightarrow Fe_3S_4 + Fe(OH)_2 + H_2. \quad (7)$$

[*Rickard and Luther*, 2007].

H_2 was evolved from all the other samples, albeit at lower contents, even though CheMin detected no FeS (Figure 11b and Table S2). Other Fe^{2+}-bearing phases are present in most of the other Gale Crater rocks and eolian sediments (e.g., olivine, magnetite, and pyroxene) that could react with water to form H_2 during SAM-EGA analysis [e.g., *Mayhew et al*., 2013]. However, FeS thermally decomposes within the SAM temperature range allowing for more complete reactions with water to form H_2 [*Yan et al*., 2008]. Only a fraction of Fe(II) silicates reacted with 50–100°C water to produce H_2 in laboratory experiments lasting up to 100 d [*Mayhew et al*., 2013]. This suggests greater H_2 production in Gale materials possessing FeS than Gale materials without FeS. The highest H_2 production from the Sheepbed JK and CB mudstones demonstrates the significantly reduced nature of these rocks and that despite possessing oxidizing phases (e.g., sulfate, nitrate, and oxychlorine), the reduced nature is preserved.

While the CB sample has reduced phases (Fe sulfides), the CB rock also has the highest oxidized nitrate and oxychlorine contents relative to all the other Gale Crater materials examined to date. These oxidized salts probably did not codeposit with the iron sulfide in the JK and CB sediments. Subsequent to lacustrine deposition, fluids, or evaporative conditions concentrated these oxidized salts in CB. The lower nitrate and oxychlorine contents in JK could be the result of being leached by postdepositional fluids high in Ca sulfate that yielded the Ca sulfate veins (~1 mm) which crosscut the JK but not the CB drill hole [*Vaniman et al*., 2014].

5.4. Kimberley Formation

SAM-EGA analysis demonstrated that the WJ sandstone had the highest CO_2 carbon content and one of the lowest nitrate contents of all the samples (Figures 14b and 15b and Tables S5 and S6). Windjana, unlike the previously analyzed RN, JK, and CB, was characterized by having equal amounts of sulfur detected by SAM-EGA and the APXS (Figure 12b and Table S3).

Windjana has the highest CO_2 carbon content (2373 ± 820 μg $C_{(CO2)}$/g) with most CO_2 being evolved at temperatures (<450°C) that are consistent with organic C. A portion of the CO_2 below 250°C could be attributed to adsorbed CO_2. Nevertheless, if half the detected CO_2 was attributed to adsorbed CO_2, there was still a substantial amount of evolved CO_2 that could be attributed to organic C. The relatively less altered nature of WJ could promote retention of organic C, especially if organic C is dominated by water-soluble organic carbon such as the carboxylic acids that are predicted to exist on the Martian surface [*Benner et al*., 2000]. Limited postdepositional aqueous processes would allow for retention of water-soluble organic carbon in WJ. Reduced organic C was not detected by SAM-EGA above background levels or by SAM-GCMS in WJ, suggesting that organic C represented by evolved CO and CO_2 could be oxidized to water-soluble organic carbon. Alternatively, the WJ source materials (parent rocks) might have had inherently high organic C relative to the other materials thus far analyzed by SAM-EGA.

Windjana has the lowest nitrate concentration in the Gale materials (Figure 14b and Table S5) analyzed by SAM suggesting that the WJ sandstone was either leached of initially deposited nitrate or that it was exposed to solutions with much less nitrate than the other Gale materials. If WJ was leached of its nitrate, then this event preceded any deposition of soluble organic C described above. The WJ O_2 and Cl contents were not the lowest of all the Gale Crater materials examined by SAM-EGA, suggesting soluble oxychlorine and chloride were deposited after nitrate was leached.

The nearly equivalent WJ SAM-S and APXS-S contents indicates that WJ has a low Ca sulfate content. This suggests that the WJ was not exposed to depositional or postdepositional fluids enriched in Ca sulfate.

Other Gale Crater samples (e.g., JK, CB, BK, BS, and GH) that have SAM-S contents less than APXS-S contents (Figure 12b and Table S3) were the result of having greater Ca sulfate inputs than what occurred in WJ. This is supported by the CheMin/APXS analysis that indicated SAM-S is dominated by X-ray amorphous Mg-SO_4-bearing phases [*Treiman et al*., 2016].

The source of this amorphous Mg-SO_4 is consistent with dehydration of hydrated crystalline Mg sulfate phases (e.g., starkeyite and hexahydrite). Laboratory analog studies have demonstrated that dehydration of crystalline-hydrated Mg sulfates leads to amorphous sulfate phases [*Chipera and Vaniman*, 2007]. The amorphous Mg-SO_4 in WJ is consistent with an initially deposited, highly hydrated crystalline Mg sulfate that subsequently dehydrated to an amorphous phase. Kieserite has been shown to be stable under vacuum conditions and is not expected to dehydrate. The geochemical conditions (e.g., ionic activities, pH, and temperature) required to form these higher hydration state Mg sulfates differs from lower hydration state (e.g., kieserite) [e.g., *Doner and Lynn*, 1989]. Thus, the geochemical conditions in the Windjana sandstones were likely not favorable for kieserite formation but may have been more favorable for other higher-hydrated Mg sulfate formation. Amorphous Fe sulfates that may be present in other samples (e.g., RN, JK, CB, and BK) suggest that similar processes could have operated where Fe sulfates with high hydration states (e.g., copiapite and melanterite) were initially deposited that subsequently dehydrated to yield amorphous Fe sulfate [e.g., *Wang and Zhou*, 2014; *Sklute et al*., 2015; *Rogers et al*., 2016]. The geochemical conditions for highly hydrated Fe sulfate formation differ from those of lower hydration state jarosite [e.g., *Spencer*, 2000; *Jambor et al*., 2000], which may provide clues to past geochemical conditions where only amorphous Fe sulfate is found and not jarosite.

5.5. Murray Formation

The Murray formation (CH, MJ, TP, and BK) mudstones were deposited in a lacustrine environment and the composition of these mudstones record a complex pH and redox geochemical history [*Hurowitz et al*., 2017; *Rampe et al*., 2017]. This record of environmental change is indicated by the presence of oxidizing (hematite), reducing (magnetite), acid (jarosite), and alkaline (apatite and phyllosilicate) mineralogies at different stratigraphic positions. The SAM-EGA analyses provided additional evidence of this complicated geochemical history as indicated by presence of oxidizing (nitrate, sulfate, and oxychlorine), and alkaline (carbonate) phases, along with evidence of organics.

Some of the lowest CO_2 yet highest CO carbon contents occur in Murray samples (Figures 15b and 16b and Tables S6 and S7), with evolution temperatures that occur mostly below 450°C, consistent with presence of organic C. No organic C fragments were detected below 450°C by SAM-EGA or SAM-GCMS above background levels suggesting that most organics are oxygen bearing, consistent with the observations of oxygen-bearing organic C in the Tissint Martian meteorite [*Steele et al*., 2014]. The CO_2 and CO contents decreased with increasing elevation (Figures 15b and 16b). This carbon content trend with elevation could simply reflect the organic C content of the initially depositing material. Though the possibility exists that prior to nitrate and oxychlorine additions the water-soluble organics were mobilized to greater depths in the Murray via leaching processes.

The BK sample has a higher nitrate content than the other Murray materials, which is attributed to the addition of a nitrate from a different source region than those that contributed sediments to the other Murray rock samples. The NO intensity and release profile between 200 and 450°C in BK are similar to CH, MJ, and TP NO releases (Figure 14a) indicating the presence of a nitrate derived from a similar source. The NO peak at 521°C in BK does not exist in the other samples and is consistent with the addition of nitrate from a different source. Nitrate was initially deposited in CH, MJ, TP, and BK from a similar source, but additional fluids containing nitrate from a different source subsequently affected BK and not the other lower Murray rocks.

The BK sample also possesses more oxychlorine than the other Murray rocks (Figure 17b and Table S8). There are variations in oxychlorine-O_2 peak temperatures between the BK and the other Murray materials but not as much as with the NO peak temperatures. Nevertheless, it appears that along with nitrate, BK was exposed to more oxychlorine than the other Murray materials.

Diagenetic complexity in the Murray formation is indicated by evidence of both acidic and alkaline fluids. A high-temperature CO_2 peak (~600°C) consistent with Mg-bearing carbonate was detected in TP and an ~800°C water peak consistent with a Mg and/or Al smectite was detected in MJ. Jarosite, a mineral that forms under acidic (~pH 2–4) conditions, was also detected in TP and MJ [*Rampe et al*., 2017]. CheMin detected ~4

and 3 wt % apatite in MJ and TP, respectively, which is not stable under acidic conditions. The detection of phases stable in acidic (jarosite) and alkaline (carbonate, phyllosilicate, and apatite) conditions may indicate changing pH conditions in a lake environment, e.g., acidic during the formation of jarosite and alkaline during diagenesis.

5.6. Stimson Formation

Notable characteristics of the Stimson materials are that they have low water and CO_2 carbon contents, have been exposed to alteration fluids that varied in pH, and have undergone a complex geochemical history characterized by elemental gains and losses [*Yen et al.*, 2017]. The low water content may be due to less adsorbed H_2O because of the coarser particles with low surface area as well as lower levels of hydrated mineralogy (e.g., phyllosilicates and hydrated salts). The nondetection of phyllosilicates and jarosite suggests that most water above 500°C could be associated with hydroxylated amorphous Al/Si phases or water inclusions trapped in amorphous and/or mineral phases.

The alteration of GH resulted in lower nitrate, oxychlorine, and organic C ($<$450°C, CO_2) in GH relative to BS (Figures 14b, 15b, and 17b and Tables S5, S6, and S8). Assuming that BS is an unaltered baseline material, organic C was lost from GH as indicated by the intensity decrease of the 345°C CO_2 peak in GH relative to BS (Figure 15a). Both CO peak intensities in BS also drop dramatically relative to GH (Figure 16a). The losses are interpreted to have been caused by leaching of these soluble salts and organic C from the rock. These losses are consistent with the alteration in GH that also resulted in feldspar and pyroxene loss [*Yen et al.*, 2017].

Although GH is characterized by chemical losses [e.g., *Frydenvang et al.*, 2016; *Yen et al.*, 2017], GH has gained sulfate. The SAM-S contents are lower than APXS-S contents in both BS and GH demonstrating that Ca sulfate-bearing fluids have infiltrated both BS and GH (Figure 12b). However, a SO_2 peak at 815°C in GH that is not present in BS (Figure 12a) likely results from addition of Mg sulfate to GH. Furthermore, the SAM-S/APXS-S content ratio is higher in GH (5.4) than BS (4.8) which is consistent with GH having more Ca sulfate than BS (Figure 12b). This is also supported by GH (7.8 ± 0.08 wt % Ca) having greater Ca content than BS (6.12 ± 0.07 wt % Ca) and GH having more anhydrite than BS [*Yen et al.*, 2017]. These results indicate that although sulfate solutions have interacted with BS, the geochemical alteration that led to GH formation also resulted in greater additions of Mg and Ca sulfate than in BS.

Along with sulfate additions, carbonate appears to have also been added to GH. The GH sample has a CO_2 release (~560°C) consistent with carbonate that is not present in BS. The level of carbonate in GH is below CheMin detection limits. The extensive alteration of GH suggests that the acid fluids were involved; however, the detection of carbonate indicates that a separate and likely later event consisting of alkaline fluids has also affected the GH material.

5.7. Implications for Habitability

The SAM instrument detections of nitrate N and organic C indigenous to Gale Crater sedimentary rocks suggest that heterotrophic microbiology could have been possible on ancient Mars. Results from this work alone cannot necessarily be used to determine if life was possible or that if life ever existed on Mars. Nevertheless, the size of microbial populations that could potentially have been supported in Gale Crater lake sediments given the detected C contents was estimated based on comparisons with observed cell densities supported by organic C in seafloor clay-dominated sediments from middle portions of the South Pacific Gyre (SPG) region [*D'Hondt et al.*, 2010, 2015]. The SPG noncalcareous sediments at Integrated Ocean Drilling Program Sites U1366 and U1369 from 0.2 to 2.2 m below the seafloor possess organic C contents of 600–2000 μgC/g. At these subseafloor horizons, microbial communities achieved cell densities that ranged from 6.2×10^3–4.8×10^5 cells/g sediment. The Gale Crater materials possess similar organic C contents (up to 2384 μg C/g; combined $C_{(CO2)}$ and $C_{(CO)}$) as these SPG sediments, supporting the notion that the extremely oligotrophic SPG microbial environment provides a useful approximation of the size of heterotrophic cell densities that could have been supported in Gale Crater, provided the organic C was bioavailable. However, factors such as radiation, hydration, and temperature fluctuations could have been significant barriers to habitability on ancient Mars. Additionally, Gale nitrate N contents (10–100 μg N/g) suggest that unlike the SPG sediments, any microbial population at Gale Crater would have likely been nitrogen limited. Due to these differences with the SPG environment along with the numerous assumptions required to extrapolate from Earth to Mars, the SPG cell densities (10^3–10^5 cells/g sediment) should be considered primarily as

a useful upper bound on what could have been possible in the putative ancient habitable environment in Gale Crater. The intent here is to demonstrate that if all necessary environmental and other essential geochemical conditions (e.g., pH, redox, and abundance other essential nutrients) were favorable for life, there was sufficient organic C to support a small microbial population similar to what is observed in the most oligotrophic environments on Earth.

6. Conclusions

Noteworthy findings specific to results of the SAM investigation are the detections of nitrate, organic C, oxychlorine phases, carbonate, and Mg sulfate. The RN, GB, GH samples possessed evolved CO_2 results consistent with carbonate indicating those samples may have been exposed to episodes of alkaline pH solutions. Oxychlorine and Mg sulfate detections in all samples, although not necessarily linked, coupled with detections made elsewhere on Mars [e.g., *Gendrin et al*., 2005; *Murchie et al*., 2009; *Hecht et al*., 2009; *Ojha et al*., 2015] demonstrate the widespread occurrence of oxychlorine and Mg sulfate phases across Mars. Water evolutions were complicated and likely derived from multiple sources including adsorbed water, interlayer and structural water from phyllosilicates, hydrated salts, jarosite hydroxyls, and mineral/glassy inclusion water. The SAM results when coupled with CheMin mineralogical and APXS geochemical analyses indicate that the sampled Gale Crater sedimentary rocks were exposed to a complicated authigenetic and diagenetic history that involved temporal (spatial?) variations in pH, redox chemistry, and salt concentration. All samples possessed oxidized phases (e.g., nitrate, oxychlorine, and sulfate), suggesting that all sediments were exposed to oxidizing conditions. However, the presence of iron sulfides [*Vaniman et al*., 2014] and reduced hydrocarbons [*Freissinet et al*., 2015] in the Sheepbed mudstone suggests that these sediments may have initially been deposited in a geochemically more reducing environment that allowed for the preservation of these reduced phases. The evolution of H_2 and H_2S from all samples also indicates that all Gale samples still possess some level of reducing potential despite the presence of oxidized phases. Organic C and nitrate detections in Gale indicate that two very important constituents for microbiology were present in Gale Crater. Although nitrogen may have been limiting, the presence of organic C suggests that heterotrophic microbiology could have been possible on ancient Mars.

Acknowledgments

The authors are grateful to the engineers and scientists of the MSL Curiosity team, who have made the mission possible and the reported data available. SAM data are publically available through the NASA Planetary Data System at: http://pds-geosciences.wustl.edu/missions/msl/sam.htm. This work was funded by support from NASA to the SAM and MSL teams. D.P.G., J.L.E., A.C.M, and C.H.H. acknowledge funding support from the NASA ROSES MSL Participating Scientist Program. C.F. acknowledges support from the NASA Postdoctoral Program, administered by Oak Ridge Associated Universities through a contract with NASA. R.N.G. acknowledges funding from Universidad Nacional Autónoma de México (DGAPA-IN109416) and Consejo Nacional de Ciencia y Tecnología de México (CONACyT 220626). The authors acknowledge the Mastcam and MAHLI operations team at Malin Space Science Systems (MSSS) for producing and providing all Mastcam mosaic and MAHLI images used in this manuscript. The authors are grateful for assistance from Deirdra M. Fey, Marie J. McBride, and Michael A. Ravine who produced the MAHLI images and MAHLI mosaics used in this manuscript. We are grateful to Steven D'hondt and Jens Kallmeyer for useful discussions regarding organic carbon data generated by the shipboard party of Integrated Ocean Drilling Program (IODP) Expedition 329 and the use of those data for comparison to Mars. We would like to thank Tanya Peretyazhko, the JGR Editor David Baratoux, the Associate Editor, and two anonymous reviewers for useful comments and edits that significantly improved this manuscript.

References

Achilles, C. N., et al. (2017), Mineralogy of an active eolian sediment from the Namib Dune, Gale Crater, Mars, *J. Geophys Res. Planets*, *122*, doi:10.1002/2017JE005262.

Agee, C. B., et al. (2013), Unique meteorite from early Amazonian Mars: Water-rich basaltic breccia Northwest Africa 7034, *Science*, *339*, 780–785, doi:10.1126/science.1228858.

Anderson, R. C., et al. (2012), Collecting samples in Gale Crater, Mars; an overview of the Mars science laboratory sample acquisition, sample processing and handling system, *Space Sci. Rev.*, *170*, 57–75.

Applin, D. M., M. R. M. Izawa, E. A. Cloutis, D. Goltz, and J. R. Johnson (2015), Oxalate minerals on Mars?, *Earth Planet. Sci. Lett.*, *420*, 127–139.

Archer, P. D., Jr., et al. (2014), Abundances and implications of volatile-bearing species from evolved gas analysis of the Rocknest aeolian deposit, Gale Crater, Mars, *J. Geophys. Res. Planets*, *119*, 237–254, doi:10.1002/2013JE004493.

Arutyunov, V. S., V. Y. Basevich, V. I. Vedeneev, O. V. Sokolov, V. A. Ushakov, and A. V. Chernysheva (1991), Kinetics of the reduction of sulfur dioxide. III: Formation of hydrogen-sulfide in the reaction of sulfur-dioxide with hydrogen, *Kinet. Catal.*, *32*, 1112–1115.

Aubrey, A., H. J. Cleaves, J. H. Chalmers, A. M. Skelley, R. A. Mathies, F. J. Grunthaner, P. Ehrenfreund, and J. L. Bada (2006), Sulfate minerals and organic compounds on Mars, *Geology*, *34*, 357–360, doi:10.1089/ast.2014.1160.

Aylmore, L. A. G., M. Karim, and J. P. Quirk (1967), Adsorption and desorption of sulfate ions by soil constituents, *Soil Sci.*, *103*, 10–15.

Benner, S. A., K. G. Devine, L. N. Matveeva, and D. H. Powell (2000), The missing organic molecules on Mars, *Proc. Nat. Acad. Sci. U.S.A.*, *97*, 2425–2430.

Berger, J. A., et al. (2016), A global Mars dust composition refined by the alpha-particle X-ray spectrometer in Gale Crater, *Geophys. Res. Lett.*, *43*, 67–75, doi:10.1002/2015GL066675.

Binns, D., and P. Marshall (1991), An ab initio study of the reaction of atomic-hydrogen with sulfur-dioxide, *J. Chem. Phys.*, *95*, 4940–4947.

Bish, D. L., et al. (2013), X-ray diffraction Results from Mars science laboratory: Mineralogy of Rocknest at Gale Crater, *Science*, *341*, doi:10.1126/science.1238932.

Blake, D. F., et al. (2013), Curiosity at Gale Crater, Mars: Characterization and analysis of the Rocknest sand shadow, *Science*, *341*, doi:10.1126/science.1239505.

Borchardt, G. (1989), Smectites, in *Minerals in Soil Environments*, edited by J. B. Dixon and S. B. Weed, pp. 675–727, SSSA, Madison.

Bowden, S. A., and J. Parnell (2007), Intracrystalline lipids within sulfates from the Haughton impact structure: Implications for survival of lipids on Mars, *Icarus*, *187*, 422–429.

Bristow, T. F., et al. (2015), Sheepbed the origin and implications of clay minerals from Yellowknife Bay, Gale Crater, Mars, *Am. Mineral.*, *100*, 824–836.

Campbell, J. H., G. Gallegos, and M. Gregg (1980), Gas evolution during oil shale pyrolysis. 1: Nonisothermal rate measurements, *Fuel*, *59*, 718–726.

Campbell, J. L., G. M. Perrett, R. Gellert, S. M. Andrushenko, N. L. Boyd, J. A. Maxwell, P. L. King, and C. D. M. Schofield (2012), Calibration of the Mars Science Laboratory Alpha Particle X-ray Spectrometer, *Space Sci. Rev.*, *170*, 319–340, doi:10.1007/s11214-0129873-5.

Cannon, K. M., B. Sutter, D. W. Ming, W. V. Boynton, and R. Quinn (2012), Perchlorate induced low temperature carbonate decomposition in the Mars phoenix thermal and evolved gas analyzer (TEGA), *Geophys. Res. Lett.*, *39*, L13203, doi:10.1029/2012GL051952.
Catling, D. C., M. W. Claire, K. J. Zahnle, R. C. Quinn, B. C. Clark, M. H. Hecht, and S. Kounaves (2010), Atmospheric origins of perchlorate on Mars and in the Atacama, *J. Geophys. Res.*, *115*, E00E11, doi:10.1029/2009JE003425.
Chipera, S. J., and D. T. Vaniman (2007), Experimental stability of magnesium sulfate hydrates that may be present on Mars, *Geochim. Cosmochim. Acta*, *71*, 241–250.
Clark, J. V., et al. (2016), The investigation of chlorate/iron-phase mixtures as a possible source of oxygen and chlorine detected by the sample analysis at Mars (SAM) instrument in Gale Crater, *Proc. Lunar Planet. Sci. Conf. 47th*, 1537 pp., The Woodlands, Tex.
Cousin, A., et al. (2015), Compositions of coarse and fine particles in Martian soils at gale: A window into the production of soils, *Icarus*, *249*, 22–42.
Dai, Z. R., and J. P. Bradley (2001), Iron-nickel sulfides in anhydrous interplanetary dust particles organic S, *Geochim. Cosmoschim. Acta*, *65*, 3601–3612.
D'Hondt, S., F. Inagaki, C. A. Alvarez Zarikian, and the Expedition 329 Scientists (2010), South Pacific gyre subseafloor life: Expedition 329 of the riserless drilling platform Papeete, Tahiti, to Auckland, New Zealand sites U1365–U1371, in *Proceedings of the Integrated Ocean Drilling Program*, vol. 329. [Available at http://publications.iodp.org/proceedings/329/329title.htm.]
D'Hondt, S., et al. (2015), Presence of oxygen and aerobic communities from seafloor to basement in deep-sea sediments, *Nat. Geosci.*, *8*, 299–304.
Dollimore, D. (1987), The thermal decomposition of oxalates. A review, *Thermochem. Acta*, *117*, 331–363.
Doner, H. E., and W. C. Lynn (1989), Carbonates, halite, sulfate, and sulfide minerals, in *Mineral in Soil Environments*, edited by J. B. Dixon and S. B. Weed, 315 pp., Soil Sci. Soc. Am., Madison.
Downs, R. T., and MSL Science Team (2015), Determining mineralogy on Mars with the CheMin X-ray diffractometer, *Elements*, *11*, 45–50.
Edgett, K. S., et al. (2012), Curiosity's Mars hand lens imager (MAHLI) investigation, *Space Sci. Rev.*, *170*, 259–317.
Ehlmann, B. L., et al. (2017), Chemistry, mineralogy, and grain properties at Namib and High Dunes, Bagnold Dune Field, Gale Crater, Mars: A synthesis of Curiosity Rover observations, *J. Geophys. Res. Planets*, *122*, doi:10.1002/2017JE005267.
Eigenbrode, J. L., et al. (2014), Decarboxylation of carbon compounds as potential source for CO_2 and CO observed by SAM at Yellowknife Bay, Gale Crater, Mars, *Proc. Lunar Planet. Sci. Conf. 45th*, 1605 pp., The Woodlands, Tex.
Espitalié, J., K. Senga Makadi, and J. Trichet (1984), Role of the mineral matrix during kerogen pyrolysis, *Org. Geochem.*, *6*, 365–382.
Ettarh, C., and A. K. Galwey (1996), A kinetic and mechanistic study of the thermal decomposition of calcium nitrate, *Thermochim. Acta*, *288*, 203–219.
Fanale, F. P., and W. A. Cannon (1974), Exchange of adsorbed H_2O and CO_2 between the regolith and atmosphere of Mars caused by changes in surface insolation, *J. Geophys. Res.*, *79*, 3397–3402.
Filiberto, J., and A. H. Treiman (2009), Martian magmas contained abundant chlorine, but little water, *Geology*, *37*, 1087–1090.
Filiberto, J., A. H. Treiman, P. A. Giesting, C. A. Goodrich, and J. Gross (2014), High-temperature chlorine-rich fluid in the Martian crust: A precursor to habitability, *Earth Planet. Sci. Lett.*, *401*, 110–115.
Flynn, G. J. (1996), The delivery of organic matter from asteroids and comets to the early surface of Mars, *Earth Moon Planet.*, *72*, 469–474.
Fraeman, A. A., B. L. Ehlmann, R. E. Arvidson, C. S. Edwards, J. P. Grotzinger, R. E. Milliken, D. P. Quinn, and M. S. Rice (2016), The stratigraphy and evolution of lower mount sharp from spectral, morphological, and thermophysical orbital data sets, *J. Geophys. Res. Planets*, *121*, 1713–1736, doi:10.1002/2016JE005095.
Fraisslera, G., M. Jöllera, T. Brunnera, and I. Obernbergera (2009), Influence of dry and humid gaseous atmosphere on the thermal decomposition of calcium chloride and its impact on the remove of heavy metals by chlorination, *Chem. Eng. Process. Process Intensif.*, *48*, 380–388.
Francois, P., C. Szopa, A. Buch, P. Coll, A. C. McAdam, P. R. Mahaffy, C. Freissinet, D. P. Glavin, R. Navarro-Gonzalez, and M. Cabane (2016), Magnesium sulfate as a key mineral for the detection of organic molecules on Mars using pyrolysis, *J. Geophys. Res. Planets*, *121*, 61–74, doi:10.1002/2015JE004884.
Franz, H. B., et al. (2014), Analytical techniques for retrieval of atmospheric composition with the quadrupole mass spectrometer of the sample analysis at Mars instrument suite on Mars Science Laboratory, *Planet. Space Sci.*, *96*, 99–114.
Freissinet, C., et al. (2015), Organic molecules in the Sheepbed mudstone, Gale Crater, Mars, *J. Geophys. Res. Planets*, *120*, 495–514, doi:10.1002/2014JE004737.
Frydenvang, J., et al. (2016), Discovery of silica-rich lacustrine and eolian sedimentary rocks in Gale Crater, Mars, *Proc. Lunar Planet. Sci. Conf. 47th*, 2349 pp., The Woodlands, Tex.
Gallagher, P. K., D. W. Johnson, and F. Schrey (1970), Thermal decomposition of iron(II) sulfates, *J. Am. Ceram. Soc.*, *53*, 666–670.
Gellert, R. et al. (2006), Chemical diversity along the traverse of the rover Spirit at Gusev crater, *Proc. Lunar Planet. Sci. Conf. 37th*, 2176 pp., League City, Tex.
Gellert, R., et al. (2015), Chemical evidence for an aqueous history at Pahrump, Gale Crater, Mars, as seen by the APXS, *Proc. Lunar Planet. Sci. Conf. 46th*, 1855 pp., The Woodlands, Tex.
Gendrin, A., et al. (2005), Sulfates in Martian layered terrains: The OMEGA/Mars Express View, *Science*, *307*, 1587–1591.
Glavin, D. P., et al. (2013), Evidence for perchlorates and the origin of chlorinated hydrocarbons detected by SAM at the Rocknest aeolian deposit in Gale Crater, *J. Geophys. Res. Planets*, *118*, 1955–1973, doi:10.1002/jgre.20144.
Gordon, S., and C. Campbell (1955), Differential thermal analysis of inorganic compounds: Nitrates and perchlorates of alkali and alkaline earth groups and subgroups, *Anal. Chem.*, *27*, 1102–1109.
Grady, M. M., A. B. Verchovsky, I. A. Franchi, I. P. Wright, and C. T. Pillinger (2002), Light element geochemistry of the Tagish lake CI2 chondrite: Comparison with CII and CM2 meteorites, *Meteorol. Planet. Sci.*, *37*, 713–735.
Grady, M. M., A. V. Verchovsky, and I. P. Wright (2004), Magmatic carbon in Martian meteorites: Attempts to constrain the carbon cycle on Mars, *Int. J. Astrobiol.*, *3*, 117–124.
Grotzinger, J. P., et al. (2014), A habitable fluvio-lacustrine environment at Yellowknife Bay, Gale Crater, Mars, *Science*, *343*, doi:10.1126/science.1242777.
Grotzinger, J. P., et al. (2015), Deposition, exhumation, and paleoclimate of an ancient lake deposit, Gale Crater, Mars, *Science*, *350*, doi:10.1126/science.aac7575.
Hecht, M. H., et al. (2009), Detection of perchlorate and the soluble chemistry of Martian soil at the phoenix lander site, *Science*, *325*, 64–67, doi:10.1126/science.1172466.
Heinrich, M. N., B. N. Khare, and C. P. McKay (2007), Prebiotic organic synthesis in early earth and Mars atmospheres: Laboratory experiments with quantitative determination of products formed in a cold plasma flow reactor, *Icarus*, *191*, 765–778.

Hochstrasser, G., and J. F. Antonini (1972), Surface states of pristine silica surfaces I. ESR studies of *Es'* dangling bonds and of CO_2-adsorbed radicals, *Surf. Sci.*, *32*, 644–664.
Hoshino, Y., T. Utsunomiya, and O. Abe (1981), The thermal decomposition of sodium nitrate and the effects of several oxides on the decomposition, *Bull. Chem. Soc. Jpn.*, *54*, 1385–1391.
Hurowitz, J. A., et al. (2017), Redox stratification of an ancient lake in Gale Crater, Mars, *Science*, *356*, doi:10.1126/science.aah6849.
Ingraham, T. R., H. W. Parsons, and L. J. Cabri (1972), Leaching of pyrrhotite with hydrochloric-acid, *Can. Metal. Q.*, *11*, 407–411.
Jambor, J. L., D. K. Nordstrom, and C. N. Alpers (2000), Metal-sulfate salts from sulfide mineral oxidation, in *Sulfate Minerals*, *Rev. Mineral. Geochem*, vol. 40, edited by C. N. Alpers, J. L. Jambor, and D. K. Nordstrom, pp. 305–350, Mineral. Soc. Am, Washington, D. C.
Jänchen, J., R. V. Morris, D. L. Bish, M. Janssen, and U. Hellwig (2009), The H_2O and CO_2 adsorption properties of phyllosilicate-poor palagonitic dust and smectites under Martian environmental conditions, *Icarus*, *200*, 463–467.
Jull, A. J. T., J. W. Beck, and G. S. Burr (2000), Isotopic evidence for extraterrestrial organic matter in the Martian meteorite, Nakhla, *Geochim. Cosmochim. Acta*, *64*, 3763–3772.
Kah, L. C., et al. (2015), Diagenetic crystal clusters and dendrites, lower Mount Sharp, Gale Crater, *Proc. Lunar Planet. Sci. Conf. 46th*, 1901 pp., The Woodlands, Tex.
Kounaves, S. P., B. L. Carrier, G. D. O'Neil, S. T. Stroble, and M. W. Claire (2014), Evidence of Martian perchlorate, chlorate, and nitrate in Mars meteorite EETA79001: Implications for oxidants and organics, *Icarus*, *229*, 206–213.
Leshin, L. A., S. Epstein, and E. M. Stolper (1996), Hydrogen isotope geochemistry of SNC meteorites, *Geochim. Cosmochim. Acta*, *60*, 2635–2650.
Leshin, L. A., et al. (2013), Volatile, isotope, and organic analysis of Martian fines with the Mars curiosity rover, *Science*, *341*, doi:10.1126/science.1238937.
Lewis, J. M. T., J. S. Watson, J. Najorka, D. Luong, and M. A. Sephton (2015), Sulfate minerals: A problem for the detection of organic compounds on Mars?, *Astrobiology*, *15*, 247–258.
Lindsay, W. L. (1979), *Chemical Equilibria in Soils*, 39 pp., The Blackburn Press, Caldwell, N. J.
Macpherson, C. G., and D. P. Mattey (1994), Carbon isotope variations of CO_2 in central Lau Basin basalts and ferrobasalts, *Earth Planet. Sci. Lett.*, *121*, 263–276.
Macpherson, C. G., D. R. Hilton, S. Newman, and D. P. Mattey (1999), CO_2, $^{13}C/^{12}C$ and H_2O variability in natural basaltic glasses: A study comparing stepped heating and FTIR spectroscopic techniques, *Geochim. Cosmochim. Acta*, *63*, 1805–1813.
Mahaffy, P. R., et al. (2012), The sample analysis at Mars investigation and instrument suite, *Space Sci. Rev.*, *170*, 401–478.
Mahaffy, P. R., P. G. Conrad, and the MSL Science Team (2015), Volatile and isotopic imprints of ancient Mars, *Elements*, *11*, 51–56.
Malin, M. C., and K. S. Edgett (2000), Sedimentary rocks of early Mars, *Science*, *290*, 1927–1937.
Mancinelli, R. L. (1996), The search for nitrogen compounds on the surface of Mars, *Adv. Space Res.*, *18*, 241–248.
Manning, C. V., C. P. McKay, and K. J. Zahnle (2008), The nitrogen cycle on Mars: Impact decomposition of near-surface nitrates as a source for a nitrogen steady state, *Icarus*, *197*, 60–64.
Manning, C. E., E. L. Shock, and D. A. Sverjensky (2013), The chemistry of carbon in aqueous fluids at crustal and upper-mantle conditions: Experimental and theoretical constraints, *Rev. Mineral. Geochim.*, *75*, 109–148.
Markowitz, M. M. (1963), A basis for the prediction of the thermal decomposition products of metal perchlorates, *J. Inorg. Nucl. Chem.*, *25*, 407–414.
Maki, J., D. Thiessen, A. Pourangi, P. Kobzeff, T. Litwin, L. Scherr, S. Elliott, A. Dingizian, and M. Maimone (2012), The Mars science laboratory engineering cameras, *Space Sci. Rev.*, *170*, 77–93.
Malin, M. C., et al. (2010), The Mars Science Laboratory (MSL) mast-mounted cameras (Mastcams) flight instruments, *Proc. Lunar Planet. Sci. Conf. 41st*, 1123 pp., The Woodlands, Tex.
Marvin, G. G., and L. B. Woolaver (1945), Thermal decomposition of perchlorates, *Ind. Eng. Chem.*, *17*, 474–476.
Mathez, E. A. (1976), Sulfur solubility and magmatic sulfides in submarine basalt glass, *J. Geophys. Res.*, *81*, 4269–4276.
Mathez, E. A., and J. R. Delaney (1981), The nature and distribution of carbon in submarine basalts and peridotite nodules, *Earth Planet. Sci. Lett.*, *56*, 217–232.
Mayhew, L. E., E. T. Ellison, T. M. McCollom, T. P. Trainor, and A. S. Templeton (2013), Hydrogen generation from low-temperature water-rock reactions, *Nat. Geosci.*, *6*, 478–484.
McAdam, A. C., et al. (2014), Sulfur-bearing phases detected by evolved gas analysis of the Rocknest aeolian deposit, Gale Crater, Mars, *J. Geophys. Res. Planets*, *119*, 373–393, doi:10.1002/2013JE004518.
McAdam, A. C., et al. (2016), Reactions involving calcium and magnesium sulfates as potential sources of sulfur dioxide during MSL SAM evolved gas analysis, *Proc. Lunar Planet. Sci. Conf. 47th*, 2277 pp., The Woodlands, Tex.
McBride, M. J., et al. (2015), Mars Hand Lens Imager (MAHLI) observations at the Pahrump Hills field site, Gale Crater, *Proc. Lunar Planet. Sci. Conf. 46th*, 2855 pp., The Woodlands, Tex.
McCollom, T. M., and W. Bach (2009), Thermodynamic constraints on hydrogen generation during serpentinization of ultramafic rocks, *Geochim. Cosmochim. Acta*, *73*, 856–875.
McEwen, A. S., et al. (2007), Mars reconnaissance Orbiter's high resolution imaging science experiment (HiRISE), *J. Geophys. Res.*, *112*, E05S02, doi:10.1029/2005JE002605.
McLennan, S. M., et al. (2014), Elemental geochemistry of sedimentary rocks at Yellowknife Bay, *Science*, *343*, doi:10.1126/science.1244734.
Meslin, P. Y., et al. (2013), Soil diversity and hydration as observed by ChemCam at Gale Crater, Mars, *Science*, *341*, doi:10.1126/science.1238670.
Migdal-Mikuli, A., and J. Hetmańczyk (2008), Thermal behavior of $[Ca(H_2O)_4](ClO_4)_2$ and $[Ca(NH_3)_6](ClO_4)_2$, *J. Therm. Anal. Calorim.*, *2*, 529–534.
Milliken, R. E., J. P. Grotzinger, and B. J. Thomson (2010), Paleoclimate of Mars as captured by the stratigraphic record in Gale Crater, *Geophys. Res. Lett.*, *37*, L04201, doi:10.1029/2009GL041870.
Ming, D. W., et al. (2014), Volatile and organic compositions of sedimentary rocks in Yellowknife Bay, Gale Crater, Mars, *Science*, *343*, doi:10.1126/science.1245267.
Minitti, M. E., et al. (2013), MAHLI at the Rocknest sand shadow: Science and science-enabling activities, *J. Geophys. Res. Planets*, *118*, 2338–2360, doi:10.1002/2013JE004426.
Mitrofanov, I. G., et al. (2014), Water and chlorine content in the Martian soil along the first 900 m of the curiosity rover traverse as estimated by the DAN instrument, *J. Geophys. Res. Planets*, *119*, 1579–1596, doi:10.1002/2013JE004553.
Morris, R. V., et al. (2006), Mössbauer mineralogy of rock, soil, and dust at Meridiani Planum, Mars: Opportunity's journey across sulfate-rich outcrop, basaltic sand and dust, and hematite lag deposits, *J. Geophys. Res.*, *111*, E12S15, doi:10.1029/2006JE002791.

Morris, R. V., et al. (2016), Silicic volcanism on Mars evidenced by tridymite in high-SiO_2 sedimentary rock at Gale Crater, *Proc. Nat. Acad. Sci. U.S.A.*, *113*, 7071–7076.
Mu, J., and D. D. Perlmutter (1981a), Thermal decomposition of inorganic sulfates and their hydrates, *Ind. Eng. Chem. Process. Des. Dev.*, *20*, 640–646.
Mu, J., and D. D. Perlmutter (1981b), Thermal decomposition of carbonates, carboxylates, oxalates, acetates, formats, and hydroxides, *Thermochim. Acta*, *49*, 207–218.
Mu, J., and D. D. Perlmutter (1982), Thermal decomposition metal nitrates and their hydrates, *Thermochim. Acta*, *56*, 253–260.
Murchie, S. L., et al. (2009), A synthesis of Martian aqueous mineralogy after 1 Mars year of observations from the Mars reconnaissance orbiter, *J. Geophys. Res.*, *114*, E00D06, doi:10.1029/2009JE003342.
Nachon, M., et al. (2017), Chemistry of diagenetic features analyzed by ChemCam at Pahrump Hills, Gale Crater, Mars, *Icarus*, *281*, 121–136.
Navarro-González, R., et al. (2013), Possible detection of nitrates on Mars by the sample analysis at Mars instrument, *Proc. Lunar Planet. Sci. Conf. 44th*, 2648 pp., The Woodlands, Tex.
Okumura, F., and K. Mimura (2011), Gradual and stepwise pyrolyses of insoluble organic matter from the Murchison meteorite revealing chemical structure and isotopic distribution, *Geochim. Cosmochim. Acta*, *75*, 7063–7080.
Ojha, L., M. B. Wilhelm, S. L. Murchie, A. S. McEwen, J. J. Wray, J. Hanley, M. Massé, and M. Chojnacki (2015), Spectral evidence for hydrated salts in recurring slope lineae on Mars, *Nat. Geosci.*, *8*, 829–832.
Paris, E., G. Giulli, and M. R. Carroll (2001), The valence and speciation of sulfur in glasses by X-ray absorption spectroscopy, *Can. Miner*, *39*, 331–339.
Parfitt, R. L., and R. S. C. Smart (1978), Mechanism of sulfate adsorption on iron-oxides, *Soil Sci. Soc. Am. J.*, *42*, 48–50.
Pavia, D. L., G. M. Lampman, and G. S. Kriz (1982), *Introduction to Organic Laboratory Techniques: A Contemporary Approach*, 492 pp., Saunders College Publishing, Philadelphia, Pa.
Pelovski, Y., and V. Petkova (1999), Investigation on thermal decomposition of pyrite part I, *J. Therm. Anal. Calorim.*, *56*, 95–99.
Pineau, F., and M. Javoy (1994), Strong degassing at ridge crests: The behaviour of dissolved carbon and water in basalt glasses at 14°N, mid-Atlantic ridge, *Earth Planet. Sci. Lett.*, *123*, 179–198.
Quinn, R. C., H. F. H. Martucci, S. R. Miller, C. E. Bryson, F. J. Grunthaner, and P. J. Grunthaner (2013), Perchlorate radiolysis on Mars and the origin of Martian soil reactivity, *Astrobiology*, *13*, 515–520.
Rampe, E. B., et al. (2017), Mineralogy of an ancient lacustrine mudstone succession from the Murray formation, Gale Crater, Mars, *Earth Planet. Sci. Lett.*, doi:10.1016/j.epsl.2017.04.021.
Rampe, E. B., R. V. Morris, P. D. Archer Jr., D. G. Agresti, and D. W. Ming (2016), Recognizing sulfate and phosphate complexes chemisorbed onto nanophase weathering products on Mars using in-situ and remote observations, *Am. Mineral.*, *101*, 678–689.
Rapin, W., et al. (2016), Hydration state of calcium sulfates in Gale Crater, Mars: Identification of bassanite veins, *Earth Planet. Sci. Lett.*, *452*, 197–205.
Rickard, D., and G. W. Luther III (2007), Chemistry of iron sulfides, *Chem. Rev.*, *107*, 514–562.
Rogers, A. D., J. Gregerson, E. C. Sklute, M. Rucks, H. B. Jensen, R. J. Reeder, and M. D. Dyar (2016), Sequestration of mixed salts in the amorphous soil fraction on Mars, *Proc. Lunar Planet. Sci. Conf. 47th*, 1736 pp., The Woodlands, Tex.
Rudloff, W. K., and E. S. Freeman (1970), Catalytic effect of metal oxides on thermal decomposition reactions. II. The catalytic effect of metal oxides on the thermal decomposition of potassium chlorate and potassium perchlorate as detected by thermal analysis methods, *J. Phys. Chem.*, *74*, 3317–3324.
Scheidema, M. N., and P. Taskinen (2011), Decomposition thermodynamics of magnesium sulfate, *Ind. Eng. Chem. Res.*, *50*, 9550–9556.
Schmidt, M. E., et al. (2014), Geochemical diversity in first rocks examined by the curiosity rover in Gale Crater: Evidence for and significance of an alkali and volatile-rich igneous source, *J. Geophys. Res. Planets*, *119*, 64–81, doi:10.1002/2013JE004481.
Schmidt, M. E., et al. (2016), APXS classification of lower Mount Sharp bedrock: Silica enrichment and acid alteration, *Proc. Lunar Planet. Sci. Conf. 47th*, 2043 pp., The Woodlands, Tex.
Schwenzer, S. P., et al. (2012), Gale Crater: Formation and post-impact hydrous environments, *Planet. Space Sci.*, *70*, 84–95.
Segura, A., and R. Navarro-González (2005), Nitrogen fixation on early Mars by volcanic lightning and other sources, *Geophys. Res. Lett.*, *32*, L05203, doi:10.1029/2004GL021910.
Sephton, M. A. (2002), Organic compounds in carbonaceous meteorites, *Nat. Prod. Rep.*, *19*, 292–311.
Sklute, E. C., H. B. Jensen, A. D. Rogers, and R. J. Reeder (2015), Morphological, structural, and spectral characteristics of amorphous iron sulfates, *J. Geophys. Res. Planets*, *120*, 809–830, doi:10.1002/2014JE004784.
Silvestro, S., D. A. Vaz, R. C. Ewing, A. P. Rossi, L. K. Fenton, T. I. Michaels, J. Flahaut, and P. E. Geissler (2013), Pervasive aeolian activity along rover Curiosity's traverse in Gale Crater, Mars, *Geology*, *41*, 483–486.
Sleep, N. H., A. Meibom, T. Fridriksson, R. G. Coleman, and D. K. Bird (2004), H_2-rich fluids from serpentinization: Geochemical and biotic implications, *Proc. Nat. Acad. Sci. U.S.A.*, *101*, 12,818–12,823.
Spencer, R. J. (2000), Sulfate minerals in evaporate deposits, in *Sulfate Minerals*, *Rev. Mineral. Geochem*, vol. 40, edited by C. N. Alpers, J. L. Jambor, and D. K. Nordstrom, pp. 173–192, Mineral. Soc. Am, Washington, D. C.
Stack, K. M., et al. (2015), Sedimentology and stratigraphy of the Pahrump Hills outcrop, lower Mount Sharp, Gale Crater, Mars, *Proc. Lunar Planet. Sci. Conf. 46th*, 1994 pp., The Woodlands, Tex.
Steele, A., M. D. Fries, H. E. F. Amundson, B. O. Mysen, M. L. Fogel, M. Schweizer, and N. Z. Boctor (2007), Comprehensive imaging and Raman spectroscopy of carbonate globules from Martian meteorite ALH 84001 and a terrestrial analogue from Svalbard, *Meteorit. Planet. Sci.*, *42*, 1549–1566.
Steele, A., et al. (2012), A reduced organic carbon component in Martian basalts, *Science*, *337*, 212–215, doi:10.1126/science.1220715.
Steele A., et al. (2014), Hydrothermal organic synthesis on Mars: Evidence from the Tissint meteorite, Meteoritics & Planetary Science, vol. *49*, A376 pp., 77th Annual Meet. Meteor. Soc., Casablanca, Morocco, 8–13 Sept.
Steele, A., F. M. McCubbin, and M. D. Fries (2016), The provenance, formation, and implications of reduced carbon phases in Martian meteorites, *Meteorit. Planet. Sci.*, *51*, 2203–2225, doi:10.1111/maps.12670.
Stern, J. S., et al. (2015), Evidence for indigenous nitrogen in sedimentary and aeolian deposits from the Curiosity rover investigations at Gale Crater, Mars, *Proc. Nat. Acad. Sci. U.S.A.*, *112*, 4245–4250.
Stern, J. C., B. Sutter, W. A. Jackson, R. Navarro-González, C. P. McKay, D. W. Ming, P. D. Archer, and P. R. Mahaffy (2017), The nitrate/(per) chlorate relationship on Mars, *Geophys. Res. Lett.*, *44*, doi:10.1002/2016GL072199.
Sutter, B., et al. (2012), The detection of carbonate in the Martian soil at the phoenix landing site: A laboratory investigation and comparison with the thermal and evolved gas analyzer (TEGA) data, *Icarus*, *218*, 290–296.

Sutter, B., et al. (2014), The investigation of chlorates as a possible source of oxygen and chlorine detected by the sample analysis at Mars (SAM) instrument in Gale Crater, Mars, *Proc. Lunar Planet. Sci. Conf. 45th*, 2136 pp., The Woodlands, Tex.

Sutter, B., et al. (2015), The investigation of perchlorate/iron phase mixtures as a possible source of oxygen detected by the sample analysis at Mars (SAM) instrument in Gale Crater, Mars, *Proc. Lunar Planet. Sci. Conf. 46th*, 2137 pp., The Woodlands, Tex.

Sutter, B., R. C. Quinn, P. D. Archer, D. P. Glavin, T. D. Glotch, S. P. Kounaves, M. M. Osterloo, E. B. Rampe, and D. W. Ming (2016), Measurements of oxychlorine species on Mars, *Int. J. Astrobiol.*, *16*, 203–217, doi:10.1017/S1473550416000057.

Tan, K. H., B. F. Hajek, and I. Barshad (1986), Thermal analysis techniques, in *Methods of Soil Analysis Part 1: Physical and Mineralogical Methods*, 2nd ed., edited by A. Klute, pp. 151–183, ASA, SSSAJ, CSA, Madison.

Thomson, B. J., et al. (2011), Constraints on the origin and evolution of the layered mound in Gale Crater, *Icarus*, *214*, 413–432.

Thompson, L. M., R. Gellert, J. G. Spray, and L. C. Kah (2015), The composition of the basal Murray formation at Pahrump Hills, Gale Crater, Mars, *Proc. Lunar Planet. Sci. Conf. 46th*, 1429 pp., The Woodlands, Tex.

Thompson, L. M., et al. (2016a), Potassium-rich sandstones within the gale impact crater, Mars: The APXS perspective, *J. Geophys Res. Planets*, *121*, 1981–2003, doi:10.1002/2016JE005055.

Thompson, L. M., M. E. Schmidt, R. Gellert, J. G. Spray, and the MSL APXS (2016b), APXS compositional trends along Curiosity's traverse, Gale Crater, Mars, *Proc. Lunar Planet. Sci. Conf. 47th*, 2709 pp., The Woodlands, Tex.

Treiman, A. H., et al. (2016), Mineralogy, provenance, and diagenesis of a potassic basaltic sandstone on Mars: CheMin X-ray diffraction of the Windjana sample (Kimberley area, Gale Crater), *J. Geophys. Res. Planets*, *121*, 75–106, doi:10.1002/2015JE004932.

Uno, T. (1951), Equilibrium between FeS and mixed gas of H_2 and H_2O, *Mem. Faculty Eng. Hokkaido Univ.*, *9*, 84–90. [Available at http://hdl.handle.net/2115/37768.]

VanBommel, S. J., et al. (2016), Deconvolution of distinct lithology chemistry through oversampling with the Mars Science Laboratory Alpha Particle X-ray Spectrometer, *X-Ray Spectrom.*, *45*, 155–161.

Vaniman, D. T., et al. (2014), Mineralogy of a mudstone at Yellowknife Bay, Gale Crater, Mars, *Science*, *343*, doi:10.1126/science.1243480.

Vasavada, A. R., et al. (2014), Overview of the Mars science laboratory mission: Bradbury landing to Yellowknife Bay and beyond, *J. Geophys. Res. Planets*, *119*, 1134–1161, doi:10.1002/2014JE004622.

Wang, A. A., and Y. H. Zhou (2014), Experimental comparison of the pathways and rates of the dehydration of Al-, Fe-, Mg- and Ca-sulfates under Mars relevant conditions, *Icarus*, *234*, 162–173, doi:10.1016/j.icarus.2014.02.003.

Westrich, H. R. (1987), Determination of water in volcanic glasses by Karl-Fischer titration, *Chem. Geol.*, *63*, 335–340.

Wilson, E. H., S. K. Atreya, R. I. Kaiser, and P. R. Mahaffy (2016), Perchlorate formation on Mars through surface radiolysis-initiated atmospheric chemistry: A potential mechanism, *J. Geophys. Res. Planets*, *121*, 1472–1487, doi:10.1002/2016JE005078.

Williams, R. M. E., et al. (2013), Martian fluvial conglomerates at Gale Crater, *Science*, *340*, 1068–1072, doi:10.1126/science.1237317.

Williams, J. T., C. K. Shearer, Z. D. Sharp, P. V. Burger, F. M. McCubbin, A. R. Santos, C. B. Agee, and K. D. McKeegan (2016), The chlorine isotopic composition of Martian meteorites 1: Chlorine isotope composition of Martian mantle and crustal reservoirs and their interactions, *Meteorol. Planet. Sci.*, *51*, 2092–2110, doi:10.1111/maps.12647.

Yan, J., L. Xu, and J. Yang (2008), A study on the thermal decomposition of coal-derived pyrite, *J. Anal. Appl. Pyrolysis*, *82*, 229–234.

Yen, A. S., et al. (2006), Nickel on Mars: Constraints on meteoritic material at the surface, *J. Geophys. Res.*, *111*, E12S11, doi:10.1029/2006JE002797.

Yen, A. S., et al. (2017), Multiple stages of aqueous alteration along fractures in mudstone and sandstone strata in Gale Crater, Mars, *Earth Planet. Sci. Lett.*, *471*, 186–198, doi:10.1016/j.epsl.2017.04.033.

Zent, A. P., and R. C. Quinn (1995), Simultaneous adsorption of CO_2 and H_2O under Mars-like conditions and application to the evolution of the Martian climate, *J. Geophys. Res.*, *100*, 5341–5349, doi:10.1029/94JE01899.